

RESEARCH ARTICLE

NHR-23 activity is necessary for *C. elegans* developmental progression and apical extracellular matrix structure and function

Londen C. Johnson¹, An A. Vo¹, John C. Clancy¹, Krista M. Myles¹, Murugesan Pooranachithra², Joseph Aguilera¹, Max T. Levenson¹, Chloe Wohlenberg¹, Andreas Rechtsteiner¹, James Matthew Ragle¹, Andrew D. Chisholm² and Jordan D. Ward^{1,*}

ABSTRACT

Nematode molting is a remarkable process where animals must repeatedly build a new apical extracellular matrix (aECM) beneath a previously built aECM that is subsequently shed. The nuclear hormone receptor NHR-23 (also known as NR1F1) is an important regulator of *C. elegans* molting. NHR-23 expression oscillates in the epidermal epithelium, and soma-specific NHR-23 depletion causes severe developmental delay and death. Tissue-specific RNAi suggests that *nhr-23* acts primarily in seam and hypodermal cells. NHR-23 coordinates the expression of factors involved in molting, lipid transport/metabolism and remodeling of the aECM. NHR-23 depletion causes dampened expression of a *nas-37* promoter reporter and a loss of reporter oscillation. The cuticle collagen ROL-6 and zona pellucida protein NOAH-1 display aberrant annular localization and severe disorganization over the seam cells after NHR-23 depletion, while the expression of the adult-specific cuticle collagen BLI-1 is diminished and frequently found in patches. Consistent with these localization defects, the cuticle barrier is severely compromised when NHR-23 is depleted. Together, this work provides insight into how NHR-23 acts in the seam and hypodermal cells to coordinate aECM regeneration during development.

KEY WORDS: *C. elegans*, Molting, NHR-23, Nuclear hormone receptor, Apical extracellular matrix, Auxin-inducible degron

INTRODUCTION

Molting is a crucial developmental process required for the growth of all ecdysozoans: a clade comprising an estimated total of 4.5 million living species (Telford et al., 2008). Invertebrate molting involves conserved processes such as apical extracellular matrix (aECM) remodeling, intracellular trafficking and oscillatory gene expression (Lažetić and Fay, 2017). Molting is also a process of interest for developing new drugs against parasitic nematodes


(Ghedini et al., 2007). Parasitic nematodes cause over a billion human infections each year and loss of livestock and crops (Ward, 2015b). However, very few drugs exist, and resistance to those drugs is emerging rapidly (Ward, 2015b). Although many genes involved in nematode molting have been identified in *C. elegans* (Frand et al., 2005), little is known about how their gene products are coordinated to promote aECM remodeling and the generation and release of a new cuticle.

Nematodes progress through four periodic larval stages (L1-L4) before becoming a reproductive adult (Brenner, 1974). The end of each larval stage is punctuated by a molt that involves trafficking and secretion of aECM components, assembly of a new aECM underneath the old cuticle, followed by separation of the cuticle from the underlying aECM (apolysis) and shedding of the old cuticle (ecdysis) (Lažetić and Fay, 2017). Apolysis coincides with a sleep-like behavior called lethargus (Singh and Sulston, 1978). The cuticle is a collagenous exoskeleton secreted by hypodermal and seam epithelial cells (Page and Johnstone, 2007). The outermost layer (glycocalyx) is rich in carbohydrates and mucins (Nelson et al., 1983; Singh and Sulston, 1978). Beneath the glycocalyx is the glycolipid- and lipid-rich epicuticle, which is postulated to function as a hydrophobic surface barrier (Blaxter, 1993; Blaxter et al., 1992). Underlying the epicuticle is a layer comprising mainly cuticlin proteins. Between the epidermal membrane and the epicuticle are collagen-rich layers, including a fluid-filled medial layer with collagen struts (Lažetić and Fay, 2017; Page and Johnstone, 2007). Sets of collagens oscillate in expression over the course of each molt and are classified into three groups based on temporal expression: early, intermediate and late collagens (Johnstone and Barry, 1996; Page and Johnstone, 2007). Although the specific localization of most collagens is unknown, collagens from the same group are thought to be in the same layer (Lažetić and Fay, 2017). A transient structure, the sheath or pre-cuticle, is formed during each larval stage and is thought to pattern the cuticle (Cohen and Sundaram, 2020). Many of the components of this pre-cuticle are related to mammalian matrix proteins. The *C. elegans* pre-cuticle contains zona pellucida proteins, proteins related to small leucine-rich proteoglycans and lipid transporters in the lipocalin family (Cohen and Sundaram, 2020; Cohen et al., 2020; Forman-Rubinsky et al., 2017; Kelley et al., 2015; Sapio et al., 2005; Vuong-Brender et al., 2017).

Nuclear hormone receptor (NHR) transcription factors are key regulators of molting in insects and nematodes (King-Jones and Thummel, 2005; Taubert et al., 2011). NHRs are characterized by a ligand-binding domain (LBD) that has the potential to bind small molecules such as ligands and dietary-derived metabolites (Taubert et al., 2011). NHRs have a canonical zinc-finger DNA-binding domain (DBD) with an unstructured hinge region between the DBD and LBD that is subject to post-translational regulation (Antebi, 2015; Campbell et al., 2008; Ward et al., 2013). A single, conserved nuclear hormone

¹Department of Molecular, Cell, and Developmental Biology, University of California Santa Cruz, Santa Cruz, CA 95064, USA. ²Department of Cell and Developmental Biology, School of Biological Sciences, University of California San Diego, La Jolla, CA 92093, USA.

*Author for correspondence (jward2@ucsc.edu)

 L.C.J., 0000-0002-8196-4957; A.A.V., 0000-0002-3130-6235; J.C.C., 0000-0003-2867-9740; K.M.M., 0000-0002-1281-7793; M.P., 0000-0003-3506-7785; J.A., 0000-0003-1824-361X; M.T.L., 0000-0002-1470-3968; C.W., 0000-0002-2848-4372; J.M.R., 0000-0002-6626-2615; A.D.C., 0000-0001-5091-0537; J.D.W., 0000-0001-9870-8936

This is an Open Access article distributed under the terms of the Creative Commons Attribution License (<https://creativecommons.org/licenses/by/4.0>), which permits unrestricted use, distribution and reproduction in any medium provided that the original work is properly attributed.

Handling Editor: Swathi Arur
Received 7 July 2022; Accepted 11 April 2023

receptor, NHR-23 (also known as NR1F1; hereafter referred to as NHR-23), which is an ortholog of DHR3 in insects and of ROR α in mammals, is a key regulator of *C. elegans* molting. NHR-23 is also necessary for spermatogenesis (Ragle et al., 2020, 2022). *nhr-23* mutation or inactivation by RNAi leads to embryonic lethality, larval arrest, ecdysis defects and morphology defects (Fränd et al., 2005; Gissendanner et al., 2004; Kostrouchova et al., 1998, 2001). *nhr-23* mRNA expression oscillates over the course of each larval stage, peaking at mid-larval stage and falling at the molt stage (Gissendanner et al., 2004; Kostrouchova et al., 2001). *nhr-23* is necessary for all four larval molts and it regulates microRNAs such as *let-7* and *lin-4* (Kostrouchova et al., 1998, 2001; Patel et al., 2022; Kinney et al., 2023 preprint). *let-7* also regulates *nhr-23*, suggesting that a feedback loop might coordinate molting with developmental timing (Patel et al., 2022). The NHR-23 insect ortholog (DHR3) is part of the molting gene regulatory network (Lam et al., 1997; Ruaud et al., 2010), and the mammalian ortholog (ROR α) regulates circadian rhythms, lipid metabolism and immunity (Jetten, 2009). However, how NHR-23 regulates molting and whether it is part of the core oscillator that promotes rhythmic gene expression over each larval stage is poorly understood (Tsiairis and Großhans, 2021).

We show here that NHR-23 protein oscillates and rapid NHR-23 depletion via an auxin-inducible degron causes severe developmental delay and death. Analysis of NHR-23 target genes suggests a role in coordinating aECM assembly, remodeling and construction of specific cuticular structures. NHR-23 depletion causes aberrant localization of the collagens ROL-6 and BLI-1, and of the pre-cuticle factor NOAH-1. NHR-23 activity is necessary in seam and hypodermal cells to promote molting and timely development. Our work reveals when and where NHR-23 acts to promote molting.

RESULTS

NHR-23 protein oscillates during development

Expression of *nhr-23* mRNA oscillates throughout each *C. elegans* larval stage (Gissendanner et al., 2004; Hendriks et al., 2014; Kostrouchova et al., 2001; Meeuse et al., 2020). However, mRNA expression profiles do not always correlate with protein levels (de Sousa Abreu et al., 2009; Vogel and Marcotte, 2012). To determine whether NHR-23 protein oscillates, we monitored the expression of an endogenously tagged NHR-23::GFP, over 28 h (*wrđ8* allele; Ragle et al., 2020). During L1, oscillating expression of NHR-23::GFP was observed in the nuclei of seam and hypodermal cells (Fig. S1). Expression of NHR-23 rises and falls before the completion of the 1st molt (Fig. 1A). As GFP tags can affect the expression or stability of proteins (Agbulut et al., 2006; Baens et al., 2006), we assayed the expression of NHR-23 through western blotting time-courses using an *nhr-23::AID*::3xFLAG* strain (*kry61* allele; Zhang et al., 2015). These experiments confirmed that NHR-23::AID*::3xFLAG also oscillates (Fig. 1B,C), similar to our NHR-23::GFP imaging experiments (Fig. 1A). We detected three distinct NHR-23 bands; the lowest band is consistent with the size of NHR-23b/f (Fig. 1B,C, Fig. S2). The upper two bands were larger than expected, which could reflect post-translational modification or that NHR-23 migrates aberrantly during SDS-PAGE. All observed NHR-23 bands oscillated, although the lowest band was expressed more strongly than the other bands (Fig. 1B,C). The peak in NHR-23 expression was earlier in each larval stage than previous qRT-PCR approaches suggested (Gissendanner et al., 2004; Kostrouchova et al., 2001) and more in line with recent RNA-seq and imaging data (Meeuse et al., 2020; Kinney et al., 2023 preprint). To understand how NHR-23 promotes molting, it is important to clarify when it peaks in expression. We examined NHR-23::GFP

expression over the course of the 4th larval stage, as vulva morphology allows for more precise sub-staging (Mok et al., 2015). NHR-23::GFP expression was first detectable in L4.1 larvae, peaked in expression from L4.2-L4.3, disappeared in the vulva by L4.5 and in the head by L4.6, and then remained undetectable (Fig. 1D,E, Fig. S1B,C), similar to what the observations of Kinney et al. (2023) of NHR-23::mScarlet.

NHR-23 depletion causes severe developmental delay

Given that NHR-23 oscillates, we tested when NHR-23 was necessary for molting during the L1 larval stage. In a pilot experiment, we consistently found weaker depletion phenotypes using an *nhr-23::GFP::AID*::3xFLAG* strain (Ragle et al., 2020) compared with the *nhr-23::AID*::3xFLAG* strain (Zhang et al., 2015) (Table S1). We therefore transitioned to using the *nhr-23::AID*::3xFLAG* strain for all experiments involving phenotypic analysis. We first tested NHR-23::AID*::3xFLAG depletion kinetics and found robust depletion within 15 min of exposure to 4 mM auxin; levels remained low over the 16 h timecourse (Fig. 2A).

We performed timed depletion experiments in the L1 larval stage (Fig. 2B) using an *eft-3p::TIR1::mRuby2* control strain (henceforth referred to as *TIR1*) and a strain that permits somatic depletion of NHR-23 in the presence of auxin (*eft-3p::TIR1::mRuby2; nhr-23::AID*::3xFLAG*; henceforth referred to as *nhr-23::AID; TIR1*). L1 larvae were synchronized by starvation arrest and release onto MYOB plates. Animals were shifted onto either 4 mM auxin or control plates every 2 h and scored for molting defects at 20 h post-release from starvation (Fig. 2B). *TIR1* control animals shifted onto control or auxin and *nhr-23::AID; TIR1* animals shifted onto control plates all reached the L2 stage (Fig. 2C,D). In contrast, *nhr-23::AID; TIR1* animals shifted onto auxin displayed multiple phenotypes, including molting defects, internal vacuoles and developmental abnormalities such as disrupted tails and viable animals with a squashed morphology (Fig. 2C). We then quantified the molting defects, scoring animals unable to shed their cuticles or with morphological abnormalities (Fig. 2D). Animals shifted onto auxin within the first 4 h post-release tended to arrest as L1 larvae with few molting or morphological defects (Fig. 2D). To determine at what stage these animals arrested, we used an *hlh-8p::GFP* promoter reporter to monitor the M cell lineage (Harfe et al., 1998). Newly hatched L1 animals have one M cell that undergoes a stereotypical series of divisions to produce 16 M lineage cells by the L1 molt (Fig. S3A) (Sulston and Horvitz, 1977). *nhr-23::AID; TIR1* animals shifted onto auxin at 3 h post-release were late reaching L1 based on M cell number (Fig. S3B,C). When NHR-23 animals were scored 72 h post-auxin shift, we observed molting defects and necrotic animals (Fig. 2E, Fig. S4A), suggestive of a severe developmental delay. We also observed arrested animals with a wild-type morphology that were likely L1 larvae by size (Fig. 2E). Shifts between 6 and 12 h post-release resulted in increased morphological and molting defects (Fig. 2D). Animals shifted onto auxin at 9 h reached the end of the L1 stage by M cell number (Fig. S3B,C). Shifts at 14 and 16 h post-release resulted in wild-type L2 animals, as judged by size (Fig. 2D).

To test whether NHR-23 was similarly required in other larval stages, we performed depletion experiments later in development during which we could use vulval morphology to score progression through the L4 stage. We performed depletion experiments shifting early L3 animals onto auxin and monitored development by scoring vulva morphology 23 h later. The majority of *TIR1* animals grown on control or auxin plates and *nhr-23::AID; TIR1* animals grown on

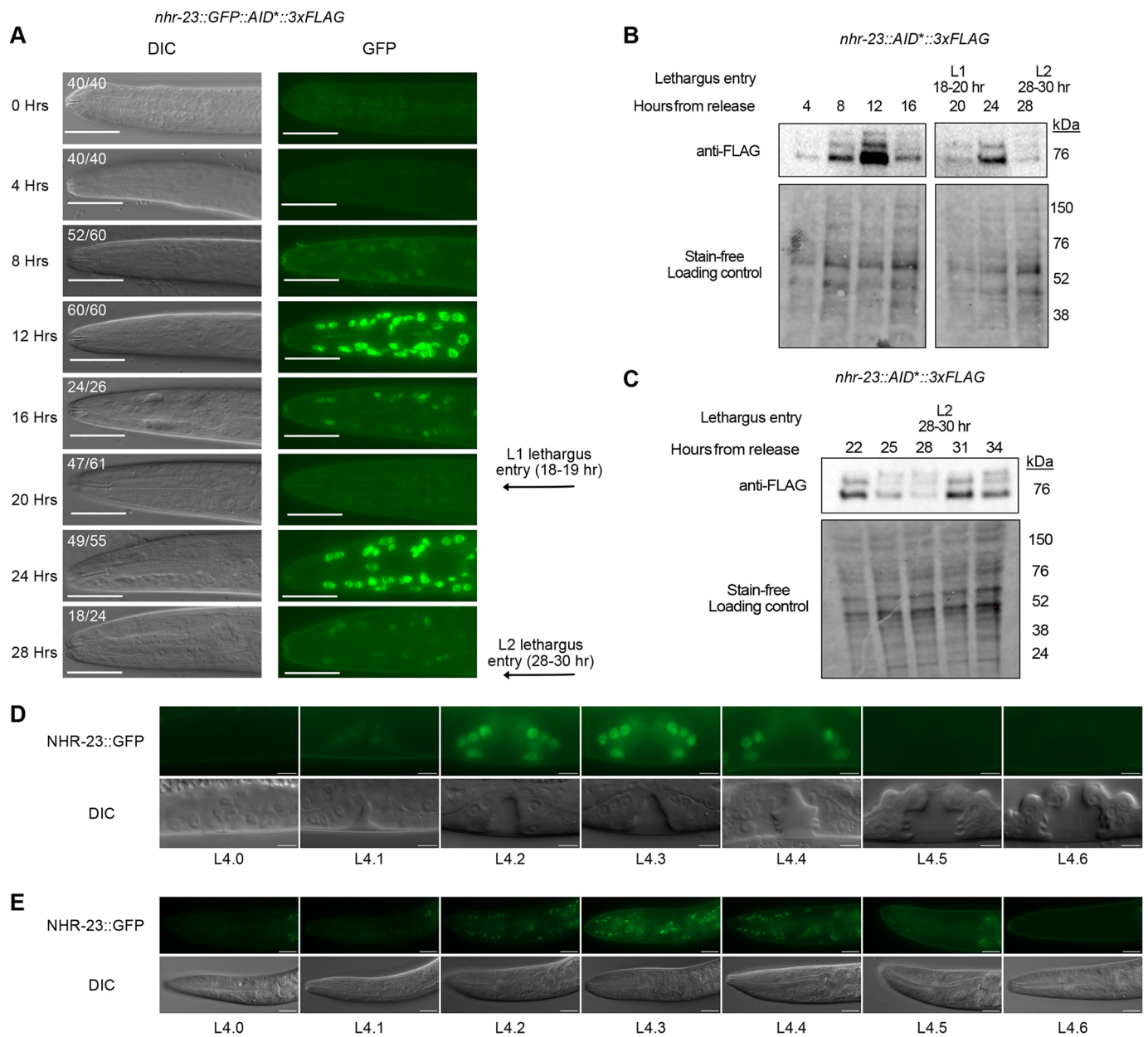


Fig. 1. NHR-23 protein oscillates during development. (A) Representative images from a timecourse monitoring the expression of endogenous NHR-23::GFP protein. Two biological replicates were performed and the images are representative of the number of animals indicated at each timepoint. Scale bars: 20 μ m. (B,C) Anti-FLAG immunoblot analysis of synchronized *nhr-23::AID*::3xFLAG* animals monitoring the expression of NHR-23 3xFLAG across two timecourses: 4-28 h (B) and 22-34 h (C). Stain-free analysis, which visualizes total protein on the membrane, is provided as a loading control. The blots are representative of three experimental replicates. The times at which animals were observed to enter lethargus is indicated in A-C. (D,E) NHR-23::GFP protein expression in the vulva (D) and head (E) during the L4 larval stage. Animals were staged based on vulval morphology (Mok et al., 2015). Images are representative of 20 animals examined over four independent experiments. Scale bars: 5 μ m in D; 20 μ m in E. *nhr-23::GFP::AID*::3xFLAG* (A,C,E) and *nhr-23::AID*::3xFLAG* (B,C) are previously described endogenous knock-ins that produce C-terminal translational fusions to all known *nhr-23* isoforms (Ragle et al., 2020; Zhang et al., 2015).

control plates reached late L4, with a fraction of the population in early or mid-L4 (Fig. 2F, Fig. S4B). In contrast, when *nhr-23::AID*; *TIR1* animals were shifted to auxin, the vast majority of animals were early L4 larvae with a fraction of the population remaining in L3 (Fig. 2F, Fig. S4B). Repeating these experiments scoring later timepoints revealed that NHR-23-depleted animals were slowly progressing through development. After 72 h on auxin, we observed adult animals, as evidenced by the presence of oocytes (Fig. 2G, Fig. S4C), while all control animals were adults. A subset of NHR-23-depleted L4 larvae could not be precisely staged due to aberrant

vulval morphology (Fig. S4C). These animals had large vulval lumens reminiscent of a 4.3 stage vulva (Mok et al., 2015), but we also observed adults with a similar large vulval lumen (Fig. S4C). A fraction of *nhr-23::AID*; *TIR1* animals grown for 72 h on auxin were dead and appeared necrotic, with large fluid filled spaces within the animal (Fig. 2G, Fig. S4C). These depletion experiments indicate that NHR-23 is required for timely developmental progression through multiple larval stages, consistent with previous reports of *nhr-23* inactivation by RNAi (Macneil et al., 2013; Patel et al., 2022).

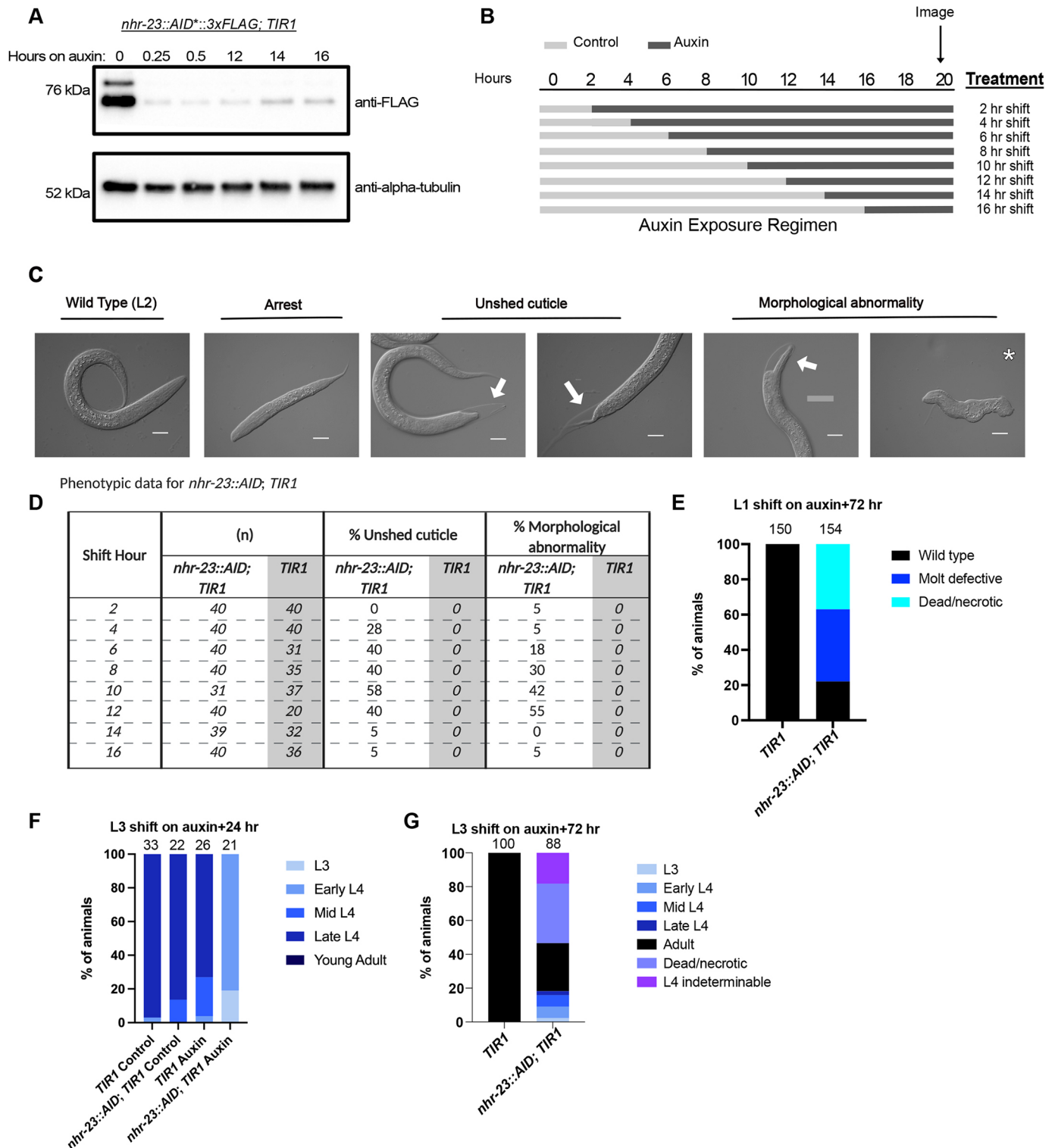


Fig. 2. Distinct phenotypes are observed when NHR-23 is depleted early or late in L1 larvae. (A) An anti-FLAG immunoblot to monitor NHR-23 depletion. Synchronized *nhr-23::AID*::3xFLAG; TIR1* and *TIR1* animals were grown on MYOB plates for 12 h and then shifted onto control or auxin plates. Lysates were collected at the indicated time points. An anti- α -tubulin immunoblot is provided as a loading control. The blots are representative of three experimental replicates. (B) Schematic of the experimental set-up. Synchronized L1 larvae were grown on control media (light-gray bands) and transferred to 4 mM auxin (dark-gray bands) every 2 h. Animals remained on auxin until they were imaged at 20 h post-release. (C) Representative images of phenotypes observed when *nhr-23::AID*::3xFLAG; TIR1* animals were exposed to auxin in the first larval stage. (D) Percentage of animals of the indicated genotypes with unshed cuticles and morphological abnormalities after exposure to auxin. The number of animals scored (*n*) is provided. (E) Synchronized *nhr-23::AID; TIR1* L1 larvae were released on auxin and scored for molting defects and death 72 h post-release. (F) Animals of the indicated genotype were synchronized and shifted onto auxin at 25 h post-release and imaged 23 h later (48 h post-release). Animals were staged based on vulval morphology (Mok et al., 2015). L4 larval stages were grouped as early L4 (4.0-4.2), mid L4 (4.3-4.5) and late L4 (4.6-4.9). (G) *nhr-23::AID; TIR1* animals were treated as in F and scored after 72 h on auxin. The number of animals assayed for each genotype and condition is indicated at the top of the graphs in E-G.

NHR-23 regulates oscillating genes involved in aECM biogenesis and regulation of protease activity

To gain insight into how NHR-23 depletion causes developmental delay, we analyzed the expression of *nhr-23*-regulated genes by mining existing microarray (Kouns et al., 2011) and oscillatory gene expression (Meeuse et al., 2020) datasets (Table S2). Of the 265 *nhr-23*-regulated genes in the microarray dataset, 236 (89%)

were oscillatory with the bulk of genes peaking in expression between 180° and 360° (Fig. 3A, Table S2); *nhr-23* mRNA peaks at 178.11° (Meeuse et al., 2020). A similar trend was observed in a recent analysis of these datasets (Tsiairis and Großhans, 2021). In contrast, 10-20% of *C. elegans* genes oscillate in expression (Hendriks et al., 2014; Kim et al., 2013; Meeuse et al., 2020) (two-tailed χ^2 test $P < 0.0001$). *nhr-23*-regulated oscillating genes

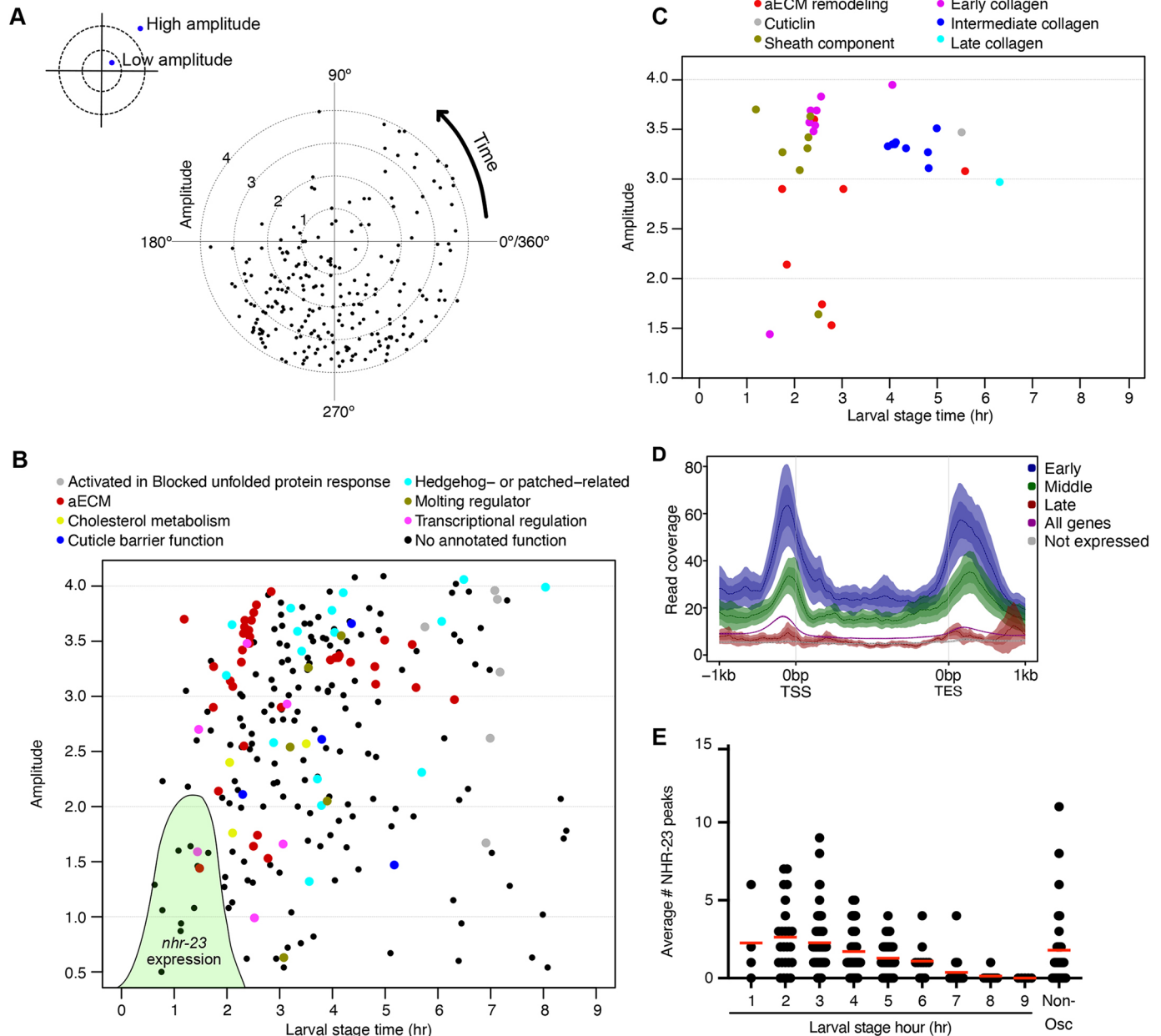


Fig. 3. NHR-23 regulates oscillating genes involved in aECM biogenesis. (A) Radar chart plotting amplitude over the phase of peak expression of *nhr-23*-regulated genes from Kouns et al. (2011). The dotted circles indicate amplitude, with the innermost circle representing an amplitude of 1 and the outermost circle representing an amplitude of 4. Created with Biorender.com. (B) The data from A plotted as a scatter plot and functionally annotated (Table S2). We converted the 360° oscillation to developmental timing over a 9 h larval stage so that 1 hour=40°. The green shaded area represents NHR-23 expression based on RNA-seq (peak phase=178.11°, amplitude=2.11; Meeuse et al., 2020), imaging (Fig. 1A,D,E) and western blotting data (Fig. 1B,C). (C) The genes in the aECM component class were subdivided into more specific classes and plotted as in B. (D) Average signal from NHR-23 ChIP-seq data (Gerstein et al., 2010) for *nhr-23*-regulated oscillating genes with peak phases at 135°-254.9° (early), 255-14.9° (middle) and 15°-134.9° (late). Expression of *nhr-23* mRNA peaks at 178.11°. Signal is plotted relative to transcription start site (TSS) and transcription end site (TES). The average NHR-23 signal for all 21,600 *C. elegans* genes (all genes) and the 20% of genes with the lowest expression (no expression) are shown for reference. The mean signal is plotted with a line and the 95% confidence interval of the mean is indicated by the shaded area. (E) Number of NHR-23 peaks flanking and within *nhr-23*-regulated genes. The genes are binned by their peak phase relative to adjusted larval stage time. Non-oscillating (non-osc) *nhr-23* genes are also depicted.

were enriched in gene ontology classes such as ‘cuticle structure’, ‘regulation of endopeptidases’ and ‘metalloprotease activity’ (Table S3). These gene ontology classes are a specific subset of the functions enriched in all oscillating genes (Table S4). To provide biological context, we converted the 360° period to developmental time, assuming a 9 h larval stage and set the molt from the start of lethargus (45°) to the end of ecdysis (135°) as in Meeuse et al. (2023). Most *nhr-23*-regulated genes involved in aECM structure/function, cholesterol metabolism, molting regulation, transcriptional regulation and signal transduction had peak amplitudes within 3 h of the *nhr-23* expression peak (Fig. 3B). Genes involved in the blocked protein unfolding response, as well as some aECM genes, peaked later in each larval stage (Fig. 3B). Although the *C. elegans* genome encodes 181 collagen genes (Teuscher et al., 2019), *nhr-23* only regulated 13 collagens, including all of the furrow collagens implicated in epidermal damage sensing; these furrow collagens are in the ‘early’ collagen group (*dpy-2*, *dpy-3*, *dpy-7* and *dpy-10*; Table S2, Fig. 3C) (Johnstone and Barry, 1996; Page and Johnstone, 2007; Dodd et al., 2018). Other *nhr-23*-regulated intermediate collagens have well-described roles in body morphology (*sqt-1*, *sqt-2* and *rol-6*; Table S2, Fig. 3C) (Kramer and Johnson, 1993; Johnstone and Barry, 1996; Page and Johnstone, 2007). There are also several sets of genes involved in aECM biogenesis and remodeling, such as lipocalins, proteases, protease inhibitors, fibrillin, PAN and zona pellucida (ZP) domain-containing proteins, and leucine-rich repeat proteins (Fig. 3C). Although not enriched as a gene ontology class, NHR-23 also regulates several transcription factors implicated in molting or energy metabolism (*peb-1*, *nhr-91* and *dpy-20*; Table S2, Fig. 3B) (Clark et al., 1995; Fernandez et al., 2004; Kasuga et al., 2013).

To explore direct targets of NHR-23, we analyzed an NHR-23 L3 ChIP-seq dataset (Gerstein et al., 2010). As expected, NHR-23 was enriched in the promoter region of genes (Fig. 3D, Fig. S5, Table S5). There was also notable enrichment downstream of the transcriptional end site (Fig. 3D, Fig. S5, Table S5). We then examined whether NHR-23 was enriched near *nhr-23*-regulated oscillating genes (Table S2). Genes that peaked in expression in the hour after the *nhr-23* mRNA peak in expression (Fig. 3E; hour 2) had the highest average number of NHR-23 peaks flanking and within their gene body. The average number of NHR-23 peaks flanking and within gene bodies declined, and few peaks were detected flanking genes between larval stage hours 7-9 (Fig. 3E). Genes that peak in expression close to when *nhr-23* mRNA levels peak tend to have higher NHR-23 levels upstream, downstream and within their gene bodies (Fig. 3D, early genes).

As NHR-23-regulated oscillating genes were enriched in proteases and protease inhibitors (Table S2), we tested how NHR-23 depletion affected expression of a *nas-37* promoter reporter; *nas-37* is a protease implicated in *C. elegans* ecdysis (Davis et al., 2004). We released synchronized *nhr-23::AID*, *TIR1* L1 larvae carrying a *nas-37p::GFP::PEST* reporter onto control and auxin plates, and monitored GFP expression over development. Animals growing on control media displayed oscillating reporter activity with peaks at 18 and 30 h (Fig. 4A,B). NHR-23 depleted animals exhibited a delayed onset of reporter expression and only a subset of animals expressed the reporter (Fig. 4A,B). There was only one pulse of *nas-37p::GFP::PEST* expression, after which we detected no reporter activity (Fig. 4A,B). Together, these data confirm that NHR-23 regulates *nas-37* expression and that, following NHR-23 depletion, there is a weaker pulse of target gene expression followed by a failure to express again.

NHR-23 is necessary for NOAH-1 localization to the aECM

Inactivation of the *nhr-23*-regulated predicted protease inhibitor gene *mlt-11* produces embryonic disorganization with accompanying lethality reminiscent of *noah-1* mutants (Ragle et al., 2022; Vuong-Brender et al., 2017). NOAH-1 is a zona pellucida domain protein that is part of the pre-cuticular aECM in embryos and larvae, a transient structure thought to play a role in patterning the cuticle and in embryonic elongation (Cohen and Sundaram, 2020). We introduced an mNeonGreen::3xFLAG (mNG::3xFLAG) tag after the ZP domain, which is similar to the insertion site for a previously generated mCherry knock-in (Fig. 5A; Vuong-Brender et al., 2017). *noah-1::mNG::3xFLAG(int)* animals had a wild-type brood size (Fig. S6A) and in *noah-1::mNG::3xFLAG(int)*, *nhr-23::AID*; *TIR1* lysates there was a band of the expected full-length protein size (~150 kDa) as well as a lower ~50 kDa band (Fig. 5B). *noah-1* is only predicted to have a single isoform so this might reflect a cleavage or degradation product. ZP proteins are frequently cleaved after their ZP domain (Gupta, 2021; Kiefer and Saling, 2002). Although there is a predicted furin RXXR cleavage site at the start of the CFCS domain, the smaller isoform is consistent with cleavage immediately after the ZP domain (Fig. 5A,B). It will be valuable in the future to create isoform-specific mNeonGreen knock-ins to determine where each localizes. NOAH-1::mNG was observed in the cuticle, and in punctate and tubular structures in the hypodermis (Fig. 5C). Hypodermal NOAH-1::mNG significantly overlapped with the lysosomal marker NUC-1::mCherry (Fig. 5C,D) (Guo et al., 2010; Clancy et al., 2023). NOAH-1::mNG was detected in lysosomes and weakly in the aECM from L4.1-L4.4, and then reached its maximum aECM intensity between L4.5 and L4.7, localizing to thick bands reminiscent of annuli (Fig. 5E). aECM expression decreased from L4.8 to young adulthood (Fig. 5E). NOAH-1::mNG also localized to alae from L4.6 onwards, similar to reports for NOAH-1::sfGFP (Katz et al., 2022).

We next examined the effect of NHR-23-depletion on NOAH-1 expression and localization. In L4 larvae, we observed the expected vulval lumen localization and aECM expression (Cohen et al., 2020; Katz et al., 2022), as well as localization to the rectum and excretory duct (Fig. 5F). NHR-23 depletion did not affect NOAH-1 localization in the excretory duct or rectum (Fig. 5F). Although vulval morphology is aberrant in NHR-23-depleted animals, NOAH-1 still localizes to cell surfaces and to lysosomes (Fig. 5F). In mid-L4, NOAH-1 is normally localized to the cuticle and lysosomes, and weakly localizes to alae (Fig. 5F). NHR-23 depletion caused a loss of NOAH-1::mNG localization to annuli, the formation of small irregular punctae and accumulation of NOAH-1::mNG in the aECM over the seam cells (Fig. 5F). Together, these data indicate that NHR-23 is dispensable for NOAH-1 expression, but necessary for correct localization in the cuticle.

NHR-23 depletion causes defects in aECM structure and function

Given the aberrant NOAH-1 localization (Fig. 5) and *nhr-23*-mediated regulation of early and intermediate collagens (Table S2), we next examined whether NHR-23 depletion affected aECM structure. We used CRISPR/Cas9-mediated genome editing in *nhr-23::AID*; *TIR1* animals to introduce mNG::3xFLAG cassettes into the intermediate collagen *rol-6* (C-terminal translational fusion) and *bli-1*, a collagen that forms struts in the adult cuticle (internal translational fusion) (Fig. 6A). We also introduced a 3xFLAG::mNG into *bli-1* at the same location as the mNG::3xFLAG knock-in. *rol-6* is regulated by *nhr-23*, whereas *bli-1* is an adult-specific

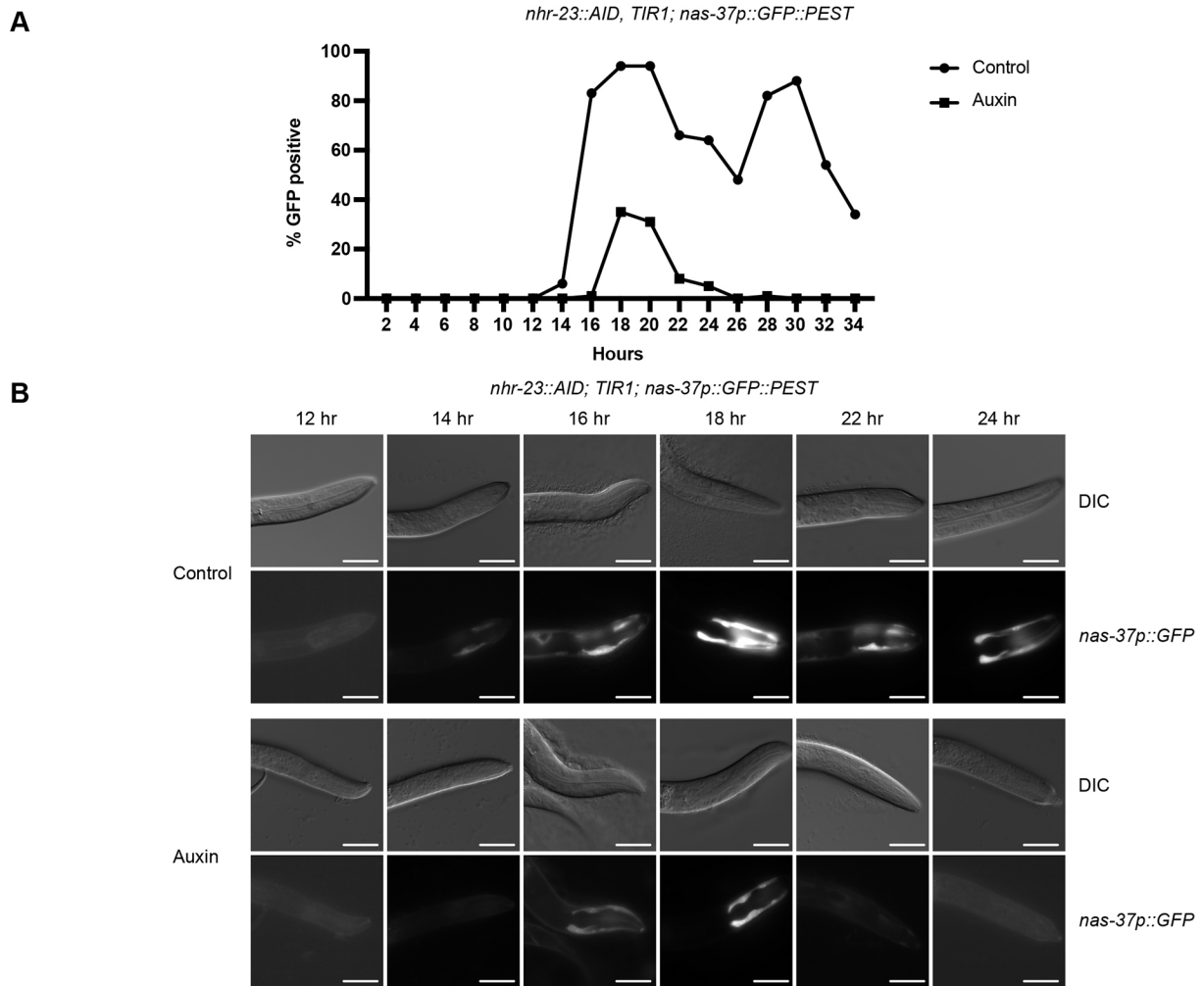


Fig. 4. NHR-23 depletion causes reduced expression of a *nas-37p::GFP::PEST* promoter reporter. (A) *nas-37p::GFP::PEST* expression timecourse. Synchronized *nhr-23::AID, TIR1; nas-37p::GFP::PEST* L1 larvae were released on control or auxin plates and scored for head or hypodermal GFP expression every 2 h. Fifty animals per time point were scored in two independent experiments and the percentage of animals expressing GFP are presented. (B) Representative images of *nhr-23::AID, TIR1; nas-37p::GFP::PEST* animals grown on control or auxin plates at the indicated time points. Scale bars: 20 μ m.

collagen expressed in L4 larvae, so its expression would not be interrogated in the microarray experiment (Table S2) (Kouns et al., 2011). We first confirmed that each knock-in had a wild-type brood size (Fig. S6A) and then tested fusion protein size by western blotting. Anti-FLAG immunoblotting on *nhr-23::AID; TIR1, rol-6::mNG::3xFLAG* lysates detected a single band of the expected size (~70 kDa; Fig. 6B). In *nhr-23::AID; TIR1, bli-1::3xFLAG::mNG*, there was a single band consistent with N-terminal processing of a monomer at an RXXR furin cleavage site that would remove 10 kDa (125 kDa predicted size). We could only detect protein by extracting soluble cuticle components. BLI-1::3xFLAG::mNG and BLI-1::mNG::3xFLAG had identical localization to one another (Fig. S6B), and were similar to an extrachromosomal transgenic BLI-1::GFP reporter (Tong et al., 2009); all subsequent experiments were performed using *bli-1::mNG::3xFLAG(int)*. Further details of BLI-1::mNG localization will be described elsewhere (Adams et al., submitted J. Adams and A.D.C., unpublished).

We first characterized expression of each translational fusion during the 4th larval stage, using vulval morphology to stage animals (Mok et al., 2015). ROL-6::mNG was first detected in thin bands reminiscent of furrows with a jagged pattern over seam cells

(L4.1-L4.3; Fig. 6D). In L4.4-L4.5, some thicker aggregations began appearing; by L4.6-L4.9, ROL-6::mNG relocated to thicker bands reminiscent of annuli (Fig. 6D). In L4.9, a fibrous pattern could also be observed (Fig. 6D). BLI-1::mNG expression was not detected until L4.5, when it was detected in hypodermal cells (Fig. 6E). In L4.4-L4.8, BLI-1::mNG was observed in a punctate localization in rows with some irregular brighter punctae (Fig. 6E). By L4.9, BLI-1::mNG was found in rows of regularly spaced punctae and was consistently excluded from the cuticle over seam cells throughout L4 and adulthood (Fig. 6E).

To examine the impact of NHR-23 depletion on BLI-1 and ROL-6 localization, we shifted *nhr-23::AID; TIR1; rol-6::mNG* or *nhr-23::AID; TIR1, bli-1::mNG* animals onto control or auxin plates in early L3. We examined animals after 23 h on control plates when animals were mid-late L4s. We scored NHR-23-depleted animals after 47 h on auxin plates due to the developmental delay; this approach ensured that control- and auxin-treated animals were stage matched. ROL-6::mNG expression appeared unaffected by NHR-23-depletion, but the furrow localization was irregular and thicker, and we observed gaps in the annular ROL-6::mNG over the seam cells (Fig. 6F). Many animals had a corset of unshed cuticle to

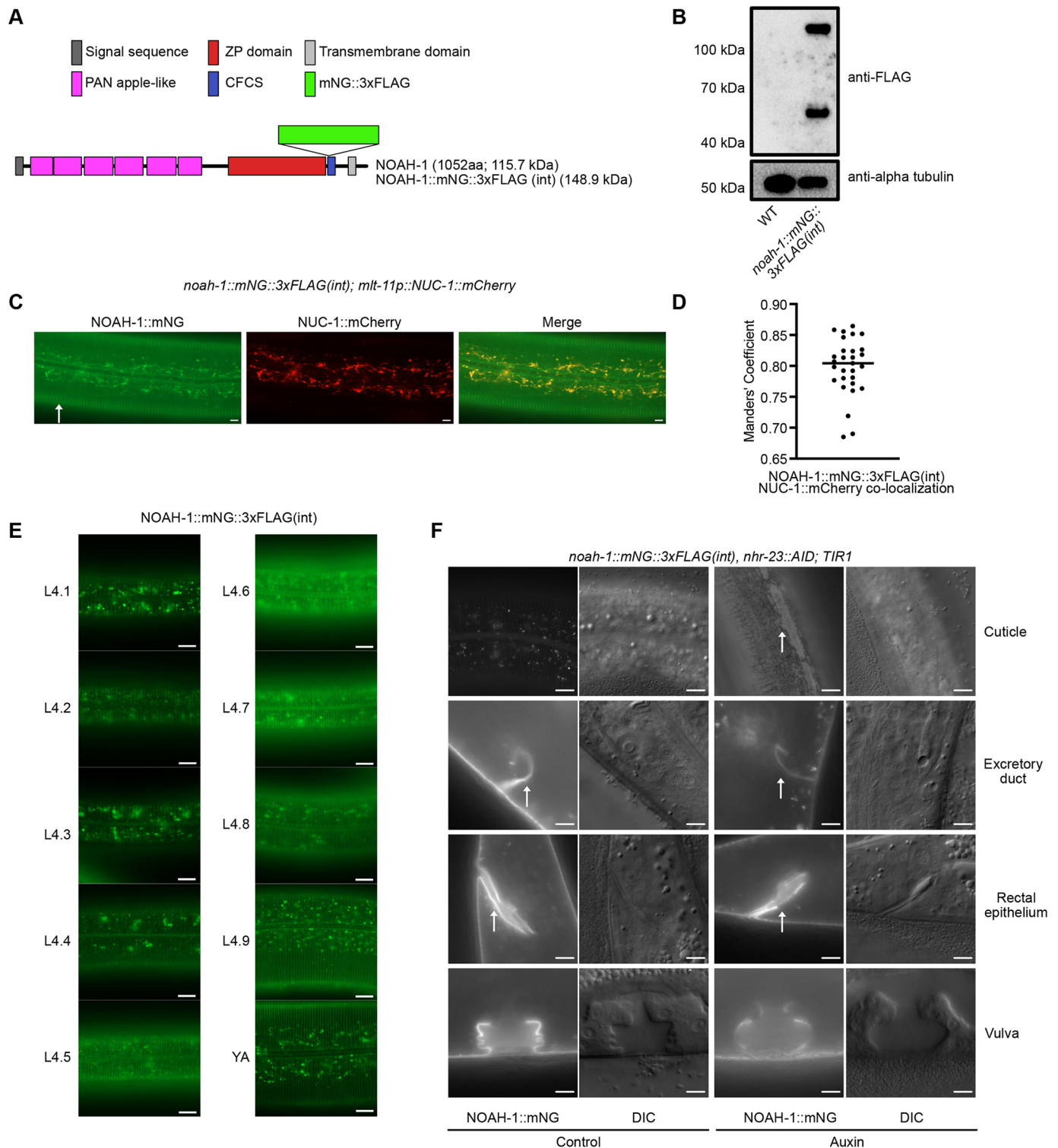


Fig. 5. NHR-23 depletion causes defective NOAH-1 localization. (A) Domain prediction for NOAH-1. ZP, zona pellucida; CFCS, consensus furin cleavage site. Predicted size of NOAH-1 and NOAH-1 with an internal mNeonGreen::3xFLAG is provided in kDa. (B) Anti-FLAG immunoblots on lysates from *noah-1::mNG::3xFLAG(int)* mid-L4 animals. An age-matched wild-type control is included in each experiment. An anti- α -tubulin immunoblot was used as a loading control. (C) Representative images from a *noah-1::mNG::3xFLAG(int); mlt-11p::NUC-1::mCherry* mid-L4 animal. Arrow indicates cuticle localization. Scale bars: 5 μ m. (D) Manders' co-localization analysis of NOAH-1::mNG::3xFLAG(int) and the lysosome marker NUC-1::mCherry. Three biological replicates were performed analyzing a total of 29 animals. The horizontal line indicates the median. (E) NOAH-1::mNG expression timecourse through L4; animals were staged by vulva morphology (Mok et al., 2015). 100 animals were examined over three independent replicates. Scale bars: 10 μ m. (F) Representative NOAH-1::mNG and DIC images of the indicated tissues of *noah-1::mNG::3xFLAG(int)* and *nhr-23::AID; TIR1* animals grown on control or auxin plates. Arrows indicate aberrant NOAH-1::mNG localization in the aECM above the seam cells, and wild-type localization to excretory duct and rectum. Two biological replicates were performed; the images represent 100% of animals scored ($n=51$ for control and $n=44$ for auxin). Scale bars: 20 μ m for all images except the *noah-1::mNG* excretory duct, rectal epithelium and vulva.

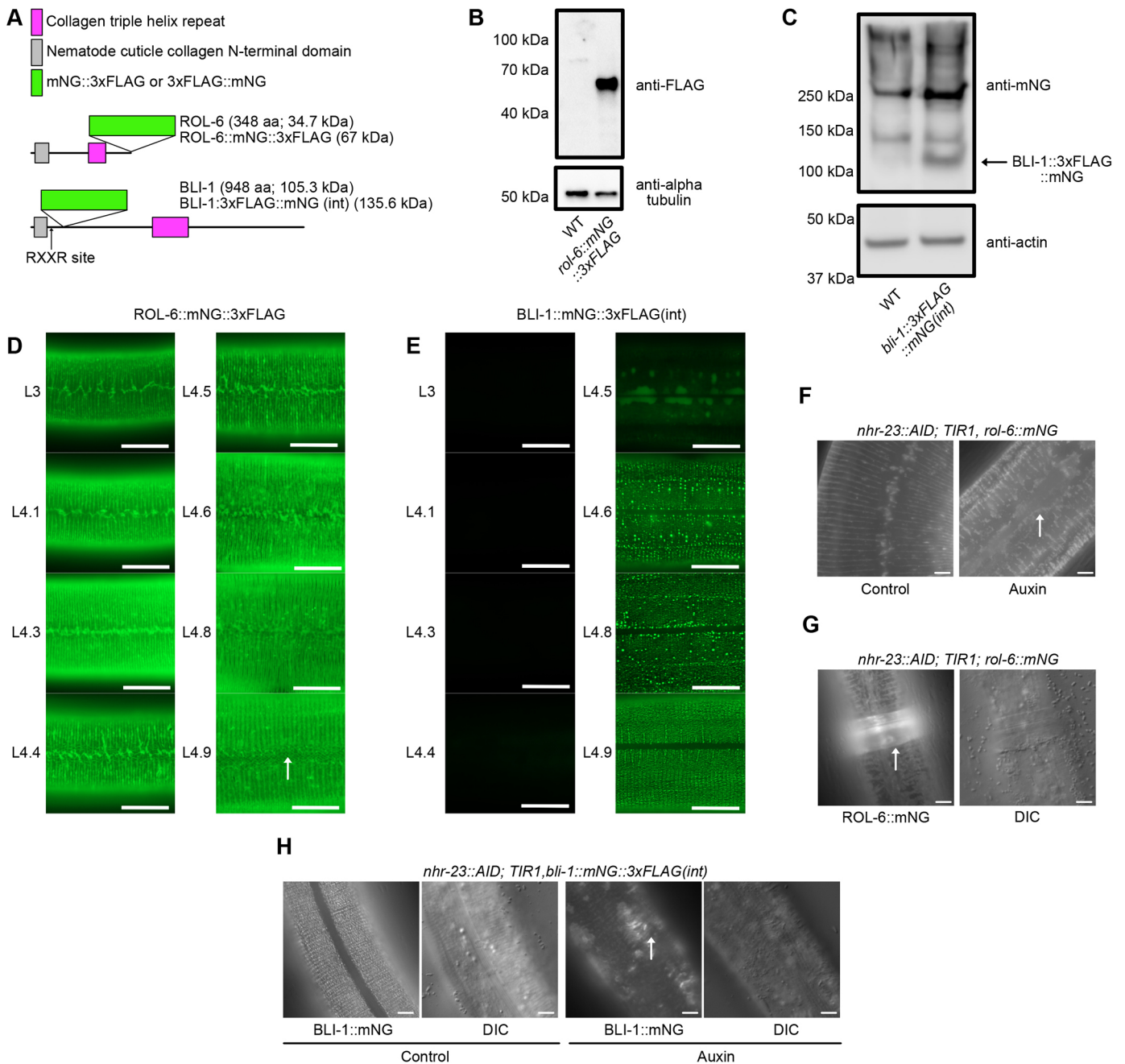


Fig. 6. NHR-23-depletion causes ROL-6 and NOAH-1 localization defect, and reduced expression and mislocalization of BLI-1. (A) Cartoon of ROL-6 and BLI-1 domains with knock-in position of mNG::3xFLAG or 3xFLAG::mNG tags. Predicted protein size is provided in kDa. (B,C) Immunoblots on lysates from *rol-6::mNG::3xFLAG* mid-L4 animals (B) and *bli-1::3xFLAG::mNG(int)* mid-L4 animals (C). An age-matched wild-type control is included in each experiment. An anti- α -tubulin (B) or anti-actin (C) immunoblot was used as a loading control. For the blots in C, the anti-mNeonGreen blot was performed on a soluble cuticle fraction and the anti-actin control was performed on a soluble intracellular fraction (see Materials and Methods). An arrow indicates the position of the BLI-1::3xFLAG::mNG band. (D) ROL-6::mNG and (E) BLI-1::mNG expression timecourse through L4; animals were staged by vulva morphology (Mok et al., 2015). One hundred animals were examined over three independent replicates. Scale bars: 10 μ m. Arrow indicates fibrous localization pattern in D. (F) Representative images of *nhr-23::AID; TIR1, rol-6::mNeonGreen::3xFLAG (rol-6::mNG)* animals grown on control or auxin plates. Arrow indicates mislocalized ROL-6::mNG in the aECM above the seam cells. Images from control and auxin-treated animals are representative of 40/40 animals observed in three independent experiments. (G) Representative images of *nhr-23::AID; TIR1, rol-6::mNG* animals grown on auxin with a corset phenotype. Corset is indicated by an arrow. 24/40 animals displayed this phenotype. (H) Representative images of *nhr-23::AID; TIR1, bli-1::mNeonGreen::3xFLAG (bli-1::mNG)* animals grown on control or auxin plates. Three experimental replicates were performed. Control images are representative of 42/42 animals scored. For auxin-treated animals, 38/38 exhibited dim expression of BLI-1::mNG and 30/38 had patchy BLI-1::mNG localization (arrow). Scale bars: 20 μ m in F-H.

which ROL-6::mNG localized (Fig. 6G). We next addressed whether NHR-23 depletion affected the formation of struts in the cuticle medial layer. NHR-23 depletion caused reduced expression of BLI-1::mNG and a loss of the punctate pattern (Fig. 6H). BLI-1::

mNG weakly localized to annuli and animals displayed bright disorganized patches of BLI-1::mNG in the cuticle (Fig. 6H). BLI-1::mNG expression appeared dimmed in the *nhr-23::AID; TIR1* background compared with a wild-type background, which would

be consistent with low level auxin-independent NHR-23 depletion (Fig. S6B).

Given the defects in aECM structure after NHR-23 depletion, we tested whether the epidermal barrier was intact. First, we incubated control and auxin-treated *nhr-23::AID*, *TIR1* animals with the cuticle-impermeable, cell membrane-permeable Hoechst 33258 dye, which stains nuclei. N2 and *TIR1* animals grown on control or auxin plates and *nhr-23::AID*, *TIR1* animals grown on control plates exhibited no staining, whereas almost all animals on auxin plates displayed Hoechst staining (Fig. 7A). Animals shifted onto auxin early or late in L1 robustly expressed an *nlp-29p::GFP* reporter (Fig. 7B, Fig. S7), which can be activated by infection, acute stress and physical damage to the cuticle (Pujol et al., 2008; Zugasti and Ewbank, 2009). We further tested the cuticle integrity in a hypo-osmotic shock assay in which animals with defective cuticle barriers rapidly die after exposure to water (Kage-Nakadai et al., 2010). *TIR1* animals grown on control media or auxin were completely viable in water (Fig. 7C). *nhr-23::AID*, *TIR1* control animals had a weakly penetrant sensitivity to hypo-osmotic shock, while the same strain grown on auxin rapidly died after hypo-osmotic shock (Fig. 7C). These data suggest that NHR-23 is required for cuticle barrier establishment or maintenance.

nhr-23 is necessary in seam and hypodermal cells for larval development

Finally, we used a tissue-specific RNAi approach to determine in which cells *nhr-23* was necessary for molting. In RNAi-proficient N2 animals, 100% of *nhr-23(RNAi)* animals exhibited developmental delay and molting defects (Fig. 8A). *nhr-23* knockdown in body-wall muscle and intestinal cells produced no molting defects and we observed only mild developmental delay (Fig. 8A). Vulval precursor cell-specific *nhr-23(RNAi)* caused moderate molting defects and developmental delay (Fig. 8A). We observed highly penetrant developmental delay and molting defects when we performed *nhr-23* RNAi in a strain using a *wrt-2* promoter for tissue-specific RNAi (Fig. 8A). *wrt-2* is expressed in seam cells,

rectal cells and hypodermal cells (Fig. S8A,B; Aspöck et al., 1999). Given this result and the defective ROL-6::mNG and NOAH-1::mNG (Figs 5 and 6) localization over seam cells, we generated more tissue-restricted RNAi strains. We used a minimal seam cell-specific enhancer with a *pes-10* minimal promoter (Ashley et al., 2021), which is robustly expressed in seam cells with some weak hypodermal expression (Fig. S8C,D). To test the specificity of this strain, we introduced a *his-72::mNG* knock-in. In animals treated with control RNAi, we observed nuclear expression in seam, hypodermal, intestinal, vulval and germline cells, as expected for a histone H3 fusion (Fig. S9). *mNeonGreen* RNAi caused reduced HIS-72::mNG expression in seam, hypodermal syncytium and intestinal nuclei. *nhr-23(RNAi)* in this *SCMp* RNAi strain phenocopied *nhr-23(RNAi)* in N2 animals with almost all animals exhibiting developmental delay and molting defects (Fig. 8A). Notably, intestine-specific *nhr-23* RNAi did not cause phenotypes (Fig. 8A). We then constructed a hypodermis-specific RNAi strain using the *semo-1* promoter (Kaletsky et al., 2018; Köhlein et al., 2020). *nhr-23* RNAi in this strain produced molting defects and developmental delay, although with less penetrance compared with our *SCMp*-specific RNAi strain (Fig. 8A). To test the effect of *SCMp*-specific *nhr-23* knockdown on the aECM, we introduced a BLI-1::mNG knock-ins in our seam cell-specific RNAi strain. *nhr-23* depletion in this strain caused reduced BLI-1 levels relative to control RNAi (Fig. 8B). This BLI-1::mNG reduction was comparable with both *nhr-23* RNAi in a wild-type control (Fig. 8B) and with NHR-23 protein depletion in the soma (Fig. 6H). Together, these data indicate that *nhr-23* is necessary in the seam and hypodermal cells for timely developmental progression, completion of molting and aECM formation.

DISCUSSION

C. elegans molting is a powerful system for understanding developmentally programmed aECM regeneration. In this study, we determine when and where NHR-23 acts to promote molting. NHR-23 oscillates and its depletion causes severe developmental

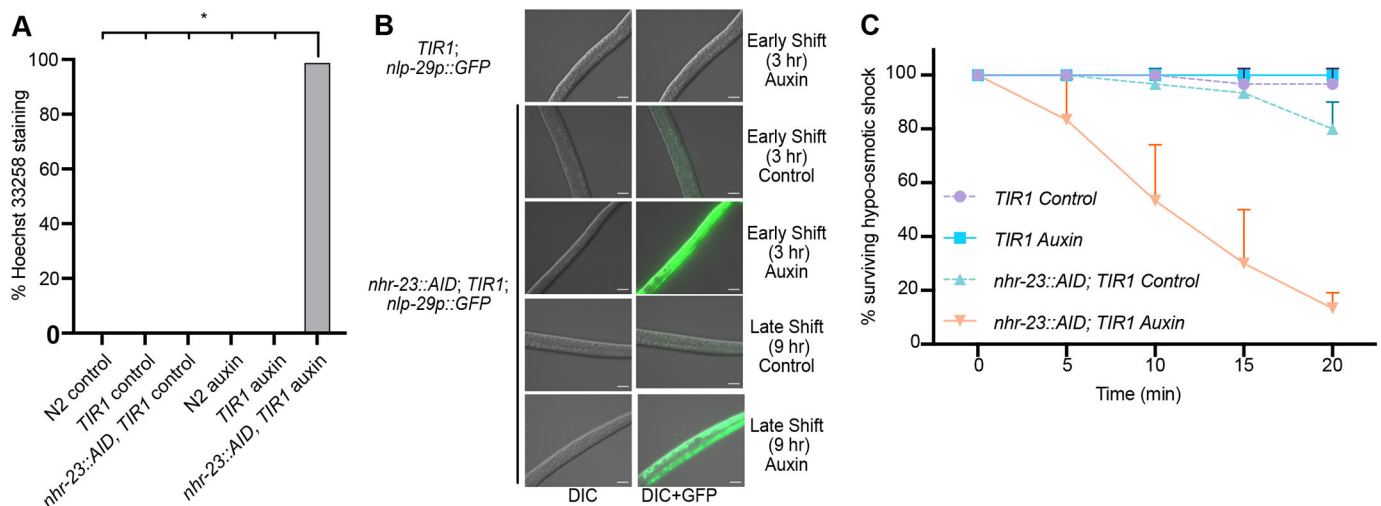


Fig. 7. Depletion of NHR-23 leads to a defective cuticle barrier. (A) Permeability to Hoechst 33258 dye. Synchronized animals of the indicated genotype were shifted onto control or auxin plates at 25 h post-release and grown for 23 h. Animals were washed off plates and incubated with the cuticle impermeable/membrane permeable Hoechst 33258 dye and scored for nuclear staining in the body. The data are from two biological replicates. * $P < 0.000001$ (two-tailed Student's *t*-test). (B) Representative images of GFP expression in animals of the indicated genotype after an early and late shift to control or auxin plates. The images are representative of 50 animals observed during each of two experimental replicates. (C) *nhr-23::AID; TIR1* and *TIR1* animals were subjected to hypo-osmotic shock and scored every 5 min. Ten animals were assayed for each genotype and condition, with three biological replicates. Data are averages of the three biological replicates \pm s.d.

A

Strain	Promoter for tissue-specific RNAi	Tissue-specific RNAi	Oscillation phase	RNAi	N	% molting defects	% developmental delay
N2	N/A	Whole animal	N/A	Control	362	0.00	0.83
				<i>nhr-23</i>	272	100.00	100.00
WM118	<i>myo-2p</i>	Body muscle	116.5°	Control	252	0.00	11.51
				<i>nhr-23</i>	320	0.00	7.50
VP303	<i>nhx-2p</i>	Intestine	Non-Osc	Control	317	0.00	12.62
				<i>nhr-23</i>	393	0.00	20.10
MGH171	<i>vha-6p</i>	Intestine	Non-Osc	Control	602	0.00	0.66
				<i>nhr-23</i>	573	0.00	0.70
JU2039	<i>lin-31p</i>	Vulval precursor cells	Non-Osc	Control	325	0.00	2.77
				<i>nhr-23</i>	367	23.43	22.07
QK52	<i>wrt-2p*</i>	Seam cell, hypodermis, rectum	263.4°	Control	299	0.00	0.33
				<i>nhr-23</i>	198	39.90	90.40
JDW371	SCMp †	Seam cell, some hypodermal, intestine	281.5°**	Control	232	0.00	0.00
				<i>nhr-23</i>	153	98.69	99.35
JDW510	<i>semo-1p</i>	Hypodermis, intestine	139.8°	Control	259	0.00	2.30
				<i>nhr-23</i>	211	69.20	62.10

**wrt-2* is an *nhr-23*-regulated gene

† SCMp is comprised of a 573 bp enhancer from the *arf-5* (formerly named *arf-3*) intronic sequence with a *pes-10Δ* minimal promoter

**oscillation phase of *arf-5*; unclear whether the enhancer oscillates in activity

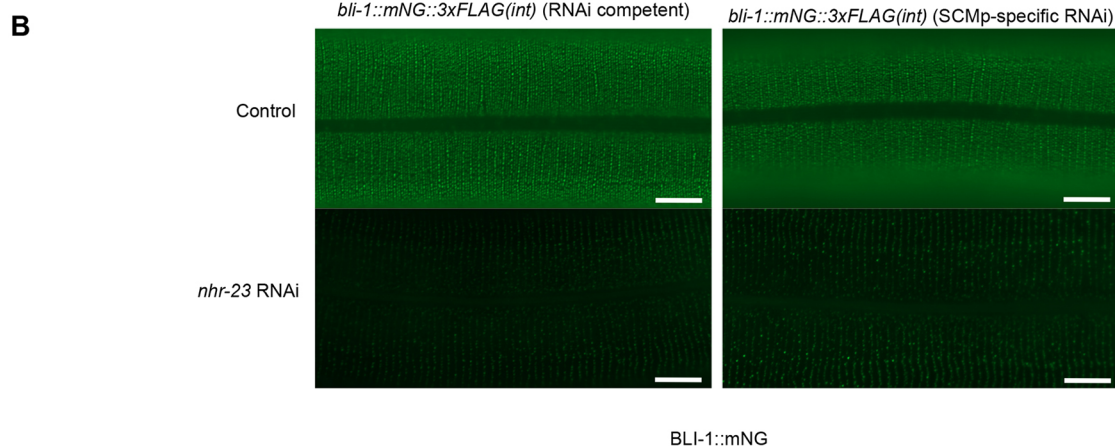


Fig. 8. *nhr-23* is necessary in seam cells for developmental progression, molting and BLI-1 localization. (A) Tissue-specific RNAi. A timed egg lay of animals of the indicated strains was performed on control or *nhr-23* RNAi plates and plates were scored 3 days later. The promoters used to reconstitute RNAi, their tissue specificity and oscillation phase (when applicable) are provided. The number of progeny scored from two biological replicates is indicated. Developmental delay was scored as a failure to reach adulthood after 72 h of growth. Molting defects included animals trapped in cuticles, animals dragging cuticles and animals with cuticle corsets. (B) L2 *bli-1::mNG* (RNAi competent) and *bli-1::mNG*; *SCMp::rde-1*; *rde-1(ne300)* (*SCMp*-specific RNAi) animals were shifted onto control or *nhr-23* RNAi plates at L2 and grown until stage L4.8. Equal exposure times were used for all images. Scale bars: 10 μ m. Images are representative of 20 animals over two independent experimental replicates.

delay. *nhr-23*-regulated genes are enriched for cuticle components and protease inhibitors, and NHR-23 is enriched at the transcription start and end sites of target genes. NHR-23 depletion causes aberrant localization of the early collagen ROL-6 and the pre-cuticle component NOAH-1. These cuticle defects are correlated with a loss of the cuticle permeability barrier function. Loss of NHR-23 function in L4 stages also causes severely reduced levels of the adult collagen BLI-1, which is also mislocalized. These cuticle defects are correlated with a loss of the cuticle barrier. Tissue-specific RNAi suggests that *nhr-23* is necessary in seam and hypodermal cells.

NHR-23 is necessary for cuticle structure and function

NHR-23 binds more robustly in the promoter and transcription end site of genes that peak in expression closer to the *nhr-23* mRNA peak in expression (Fig. 3). One intriguing possibility is that the earlier NHR-23-regulated genes may be more sensitive to NHR-23 levels. Consistent with this model, there appear to be more NHR-23 peaks flanking and within early *nhr-23*-regulated genes (Fig. 3,

Tables S2, S5). This model would align with *E. coli* amino acid biosynthesis gene regulation where enzymes earlier in the pathway have more responsive promoters with higher activity (Zaslaver et al., 2004). Interestingly, the non-oscillating *nhr-23*-regulated genes had a range in number of NHR-23 peaks. It is unclear why NHR-23 oscillation is failing to drive oscillation of these target genes. Some possible explanations include more stable mRNA transcripts in comparison with the transcripts of the oscillating genes or combinatorial gene regulation involving a non-oscillating transcription factor.

NHR-23 regulates the expression of *nas-37*, a protease implicated in molting (Fig. 4; Frand et al., 2005). Curiously, two other targets (*noah-1* and *rol-6*) seemed to be expressed at near wild-type levels but displayed aberrant localization (Figs 5 and 6). These data highlight a potential limitation of a single timepoint gene expression study. A shift in phase of an oscillating gene without change in amplitude could create the appearance of up- or downregulation, depending on the timepoint sampled (Tsiairis and Großhans, 2021).

The *nhr-23(RNAi)* microarray is a useful starting point to understand how NHR-23 promotes molting, but an RNA-seq timecourse on NHR-23 depleted animals may be necessary to identify regulated genes. Such an approach was necessary to determine how the pioneer factor, BLMP-1, promotes developmental timing (Hauser et al., 2022 preprint).

NHR-23 depletion caused aberrant localization of NOAH-1 and ROL-6, lower levels of BLI-1 and a severe barrier defect (Figs 5-7). There are numerous *nhr-23*-regulated genes that are implicated in the epithelial barrier. The cuticle furrow formed by six *nhr-23*-regulated collagens (*dpy-2*, *dpy-3*, *dpy-7*, *dpy-8*, *dpy-9* and *dpy-10*) is thought to be monitored by a sensor that coordinates several stress responses (Dodd et al., 2018). An RNAi screen of 91 collagens found that inactivation of only these six collagens caused a barrier defect (Sandhu et al., 2021). Inactivation of a subset of the furrow collagens causes permeability to Hoechst 33458 dye and elevated *nlp-29p::GFP* reporter activity (Dodd et al., 2018), consistent with our NHR-23-depletion data (Fig. 7). *bus-8* is a predicted glycosyltransferase that plays a role in the epithelial barrier and is also regulated by *nhr-23*; its peak expression follows that of the furrow collagens (Table S2). Screening *nhr-23*-regulated genes may reveal other genes implicated in the epithelial barrier and the peak phase could provide insight into how this barrier is constructed.

NHR-23-depletion causes developmental delay and failed molting

What is driving NHR-23-depleted animals to eventually attempt to molt? One model is that NHR-23 depletion is incomplete and the remaining NHR-23 is sufficient to drive low levels of target gene expression. Consistent with this idea, NHR-23 depletion or knockdown results in developmental delay but not an arrest (Fig. 2; MacNeil et al., 2013; Patel et al., 2022). Low sustained NHR-23-levels could eventually allow the accumulation of factors that initiate apolysis but with insufficient expression for execution. Consistent with this idea, an NHR-23-regulated promoter reporter (*nas-37p::GFP::PEST*) peaked at a similar time in control and NHR-23-depleted animals (Fig. 4), but was expressed at lower levels. *nas-37* is necessary for *C. elegans* ecdysis and recombinant NAS-37 promotes the formation of retractile rings, a structure associated with molting, in the parasitic nematode *H. contortus* (Davis et al., 2004). Alternatively, other factors could eventually promote molting. Molting can be uncoupled from the stage-specific developmental events controlled by the heterochronic pathway, which leads to death when animals attempt molting before completion of cell division and differentiation (Ruaud and Bessereau, 2006). Molting is thought to be controlled by a recently discovered oscillator, although the mechanism remains to be fully elucidated (Tsiarris and Großhans, 2021). It is possible that other candidate components of this oscillator, such as BLMP-1, GRH-1, NHR-25, MYRF-1 or BED-1, could eventually drive animals to molt in the absence of NHR-23 (Hauser et al., 2022 preprint; Meeuse et al., 2023; Stec et al., 2021; Stojanovski et al., 2022).

nhr-23 is necessary in seam and hypodermal cells to promote molting

Seam cell-enriched *nhr-23* RNAi caused severe developmental delay and molting defects (Fig. 8). Hypodermal-enriched *nhr-23* knockdown produced less penetrant phenotypes (Fig. 8). The most severe defects in ROL-6 and NOAH-1 localization occur above the seam cells (Figs 5 and 6). Determining how NHR-23 regulates BLI-1 expression and formation of struts will provide insight into aECM

assembly. *nhr-23* is expressed in other epidermal cells that produce the pre-cuticle and cuticle, such as vulval precursor cells, rectal cells and excretory duct cells. NHR-23 depletion did not produce obvious defects in localization of the pre-cuticle component NOAH-1 in these cells (Fig. 5). We did not see phenotypes such as excretory duct or pore lumen dilation, which would be indicative of excretory system defects (Gill et al., 2016). We observed vulval morphology defects after NHR-23 depletion, but it is not clear whether that is due to NHR-23 regulation of this specialized aECM or whether it is the consequence of developmental delay and failure to molt. Tissue-specific RNAi or protein depletion will be required to determine whether NHR-23 activity is necessary in these epithelial cells or whether it predominantly functions in seam and hypodermal cells. Our data indicate the importance of tissue-specific RNAi strain validation. *SCMp* drove reporter expression robustly in seam cells (Fig. S8). However, when we made a tissue-specific RNAi strain using *SCMp*, we observed depletion in seam, hypodermal and intestinal cells (Fig. S9). RNAi has an inherent amplification of dsRNA triggers by RNA-dependent RNA polymerases (Zhang and Ruvkun, 2012). Weak promoter activity in undesired tissues could reconstitute RNAi in these tissues. A systematic analysis of tissue-specific RNAi strains is an important future direction for interpreting studies using these strains.

Future perspectives

This work highlights the power of timed protein depletion for dissecting the role of oscillating developmental regulators in development. As transcription factors coordinate the expression of batteries of genes in a given biological process, future work will reveal how NHR-23 coordinates apical ECM remodeling, apolysis and ecdysis.

MATERIALS AND METHODS

C. elegans strains and culture

C. elegans strains (see Table 1) were cultured as originally described (Brenner, 1974), except worms were grown on MYOB instead of NGM. MYOB was made as previously described (Church et al., 1995). Animals were cultured at 20°C for all assays, unless otherwise indicated. For general strain propagation, animals were grown at 15°C according to standard protocols. Brood sizes were controlled by picking L4 larvae to individual wells of a six-well plate seeded with OP50 and incubating the plate at 20°C. Animals were transferred to new plates daily over 4 days. Two days post-transfer, the number of hatched progeny and unfertilized eggs were scored.

Genome editing and transgenesis

mNeonGreen::3xFLAG knock-ins into *bli-1*, *noah-1* and *rol-6*, and *mNeonGreen* knock-ins into *his-72* were generated by injection of Cas9 ribonucleoprotein complexes [700 ng/μl Alt-R S.p. Cas9 Nuclease V3 (IDT), 115 ng/μl crRNA and 250 ng/μl IDT tracrRNA] and a dsDNA repair template (25-50 ng/μl) created by PCR amplification of a plasmid template (Paix et al., 2014, 2015). The *bli-1* and *noah-1* knock-ins were internal and the *mNG::3xFLAG* cassette was flanked by flexible glycine- and serine-rich linker sequences. Generation of the *BLI-1::3xFLAG::mNG(int)* used in Fig. 6C will be described elsewhere (J. Adams and A.D.C., unpublished). The C-terminal *rol-6::mNG::3xFLAG* fusion encoded a flexible linker between the end of *rol-6* and the start of mNG. The *noah-1::mNG::3xFLAG(int)* knock-in used a pJW2332 repair template, which will be described elsewhere (J.M.R. and J.D.W., unpublished). The PCR products were melted to boost editing efficiency, as previously described (Ghanta and Mello, 2020). crRNAs used are provided in Table S6. Oligonucleotides used for repair template generation from template pJW2172 (Ashley et al., 2021) and for genotyping are provided in Table S7. Plasmids used are provided in Table S8. To generate JDW371 and JDW510 (seam cell and hypodermal-specific tissue-specific RNAi), we crossed a *jsTi1493* landing pad for recombination-mediated cassette exchange

Table 1. Strains used in this study

Strain	Construction	Genotype
CZ27591	Microinjection	<i>bli-1(ju1789[bli-1::3xFLAG::mNG(int)]) II</i>
JDW29	Ragle et al. (2020)	<i>nhr-23(wrd8[nhr-23::GFP^{AID}::3xFLAG]) I</i>
JDW180	Microinjection	<i>wrdEx12[SCMp::NLS-mScarlet (dpi)-tbb-2 3'UTR+pCFJ90 (myo-2p::mCherry)]</i>
JDW258	Ashley et al. (2021)	<i>wrdSi22 [eft-3p::TIR1::F2A::mTagBFP2::AID*::NLS::tbb-2 3'UTR+SEC, l:-5.32], nhr-23(kry61(nhr-23::AID*-TEV-3xFLAG)) I</i>
JDW259	Ashley et al. (2021)	<i>wrdSi55[eft-3p::TIR1::F2A::mTagBFP2::AID*::NLS::tbb-2 3'UTR, l:-5.32], nhr-23(kry61(nhr-23::AID*-TEV-3xFLAG)) I</i>
JDW322	Microinjection	<i>wrdEx29[wrt-2p::NLS-mScarlet (dpi)-tbb-2 3'UTR]</i>
JDW348	Crossing	<i>ieSi57 [Peft-3::TIR1::mRuby::unc-54 3'UTR, cb-unc-119(+)] II; frIs7 [nlp-29p::GFP+col-12p::DsRed] IV</i>
JDW349	Crossing	<i>nhr-23(kry61(nhr-23::AID*-TEV-3xFLAG)) I; ieSi57 [Peft-3::TIR1::mRuby::unc-54 3'UTR, cb-unc-119(+)] II; frIs7 [nlp-29p::GFP+col-12p::DsRed] IV.x</i>
JDW330	Crossing	<i>jsTi1493 [mosL loxP mex-5p FLP sl2 mNeonGreen rpl-28p FRT GFP-HIS-58 FRT3 mosR] IV; rde-1 (ne300) V</i>
JDW354	Crossing	<i>wrdSi60[eft-3p::TIR1::F2A::mTagBFP2::AID*::NLS::tbb-2.tbb-2 3'UTR, l:-5.32] I; ayls6 [hlh-8::GFP fusion+dpv-20(+)] X</i>
JDW355	Crossing	<i>wrdSi61[eft-3p::TIR1::F2A::mTagBFP2::AID*::NLS::tbb-2.tbb-2 3'UTR, l:-5.32], nhr-23(kry61(nhr-23::AID*-TEV-3xFLAG)) I; ayls6 [hlh-8::GFP fusion+dpv-20(+)] X</i>
JDW356	Crossing	<i>wrdSi59[eft-3p::TIR1::F2A::mTagBFP2::AID*::NLS::tbb-2 3'UTR, l:-5.32], daf-16(mu86) I; ayls6 [hlh-8::GFP fusion+dpv-20(+)] X</i>
JDW357	Crossing	<i>wrdSi59[eft-3p::TIR1::F2A::mTagBFP2::AID*::NLS::tbb-2 3'UTR, l:-5.32], nhr-23(kry61(nhr-23::AID*-TEV-3xFLAG)), daf-16(mu86) I; ayls6 [hlh-8::GFP fusion+dpv-20(+)] X</i>
JDW370	Microinjection	<i>jsTi1493 [mosL::loxP::mex-5p::FLP::sl2::mNeonGreen::rpl-28p::FRT [wrdSi64(SEC::loxP::SCMp::rde-1 CDS+3'UTR)] FRT3::mosR] IV; rde-1 (ne300) V</i>
JDW371	SEC excision of JDW370	<i>jsTi1493 [mosL loxP [wrdSi65(SCMp::rde-1 CDS+3'UTR)] FRT3::mosR] IV; rde-1 (ne300) V</i>
JDW376	Clancy et al. (2023)	<i>jsTi1493 {mosL::loxP::mex-5p::FLP::sl2::mNeonGreen::rpl-28p::FRT [wrdSi67(SEC::loxP::mlt-11p (-2.8 kb)::nuc-1::mCherry-tbb-2 3'UTR)] FRT3::mosR} IV</i>
JDW389	Microinjection	<i>bli-1(wrd84[bli-1::mNG::3xFLAG(int)]) II</i>
JDW395	Crossing	<i>wrdSi73[eft-3p::TIR1::F2A::mTagBFP2::AID*::NLS::tbb-2 3'UTR], nhr-23(kry61(nhr-23::AID*-TEV-3xFLAG)) I; oxIs134[Pnas-37::GFP:rODC(pest)(pWD95@90 ng/ul),lin-15(+)]</i>
JDW459	Microinjection	<i>nhr-23(kry61(nhr-23::AID*-TEV-3xFLAG)) I; ieSi57 [Peft-3::TIR1::mRuby::unc-54 3'UTR, cb-unc-119(+)] II</i>
JDW460	Microinjection	<i>noah-1(wrd119[noah-1::internal mNeonGreen (dpi)::3xFLAG::linker]) I</i>
JDW463	Microinjection	<i>nhr-23(kry61(nhr-23::AID*-TEV-3xFLAG)) I; ieSi57 [Peft-3::TIR1::mRuby::unc-54 3'UTR, cb-unc-119(+)], bli-1(wrd122[bli-1::internal linker::mNeonGreen (dpi)::3xFLAG::linker]) II</i>
JDW472	Microinjection	<i>rol-6(wrd123[rol-6::C-term mNeonGreen (dpi)::3xFLAG::linker]) I; jsTi1493 wrdSi65[SCMmin::pes-10delta::rde-1 CDS+3'UTR in pLF3FShC] IV; rde-1 (ne300) V</i>
JDW475	Microinjection	<i>noah-1(wrd126[noah-1::internal linker::mNeonGreen (dpi)::3xFLAG::linker]), nhr-23(kry61(nhr-23::AID*-TEV-3xFLAG)) I; ieSi57 [Peft-3::TIR1::mRuby::unc-54 3'UTR, cb-unc-119(+)] II</i>
JDW509	Microinjection	<i>jsTi1493 [mosL::loxP::mex-5p::FLP::sl2::mNeonGreen::rpl-28p::FRT [wrdSi96(SEC::loxP::semo-1 (Y37A1B.5)p::rde-1 CDS+3'UTR)] FRT3::mosR] IV; rde-1 (ne300) V</i>
JDW510	SEC excision of JDW509	<i>jsTi1493 [mosL loxP [wrdSi97(semo-1p::rde-1 CDS+3'UTR)] FRT3::mosR] IV; rde-1 (ne300) V</i>
JDW525	Microinjection	<i>his-72(wrd142[mNeonGreen::his-72]) III; jsTi1493 [mosL loxP [wrdSi65(SCMp::rde-1 CDS+3'UTR)] FRT3::mosR] IV; rde-1 (ne300) V</i>
JDW537	Cross of JDW376xJDW460	<i>noah-1(wrd119[noah-1::internal mNeonGreen (dpi)::3xFLAG::linker]) I; jsTi1493 wrdSi67[mosL::loxP::mex-5p::FLP::sl2::mNeonGreen::rpl-28p::FRT [wrdSi67(SEC::loxP::mlt-11p (-2.8 kb)::nuc-1::mCherry-tbb-2 3'UTR)] FRT3::mosR] IV</i>
JDW538	SEC excision of JDW537	<i>noah-1(wrd119[noah-1::internal mNeonGreen (dpi)::3xFLAG::linker]) I; jsTi1493 wrdSi104[mosL::loxP::mlt-11p (-2.8 kb)::nuc-1::mCherry-tbb-2 3'UTR)] FRT3::mosR] IV</i>
KRY87	Zhang et al. (2015)	<i>nhr-23(kry61(nhr-23::AID*-TEV-3xFLAG)) I</i>
KRY88	Zhang et al. (2015)	<i>nhr-23(kry61(nhr-23::AID*-TEV-3xFLAG)) I; ieSi57 [Peft-3::TIR1::mRuby::unc-54 3'UTR, cb-unc-119(+)] II</i>
NM5179	Nonet (2020)	<i>jsTi1493 [mosL loxP mex-5p FLP sl2 mNeonGreen rpl-28p FRT GFP-HIS-58 FRT3 mosR] IV</i>

Strains provided by the *Caenorhabditis* Genetics Center

Strain	Genotype
N2	Wild type
CA1200	<i>ieSi57 [Peft-3::TIR1::mRuby::unc-54 3'UTR, cb-unc-119 (+)] II</i> (Zhang et al., 2015)
CF1038	<i>daf-16(mu86) I</i> (Lin et al., 1997)
PD4666	<i>ayls6 [hlh-8::GFP fusion+dpv-20(+)] X</i> (Harfe et al., 1998)
QK52	<i>rde-1(ne219) V; xkIs99[wrt-2p::rde-1::unc-54 3'UTR]</i> (Melo and Ruvkun, 2012)
VP303	<i>rde-1(ne219) V; kbls7[lnhx-2p::rde-1+rol-6(su1006)]</i> (Espelt et al., 2005)
JU2039	<i>mfls70 [lin-31p::rde-1+myo-2p::GFP] IV; rde-1(ne219) V</i> (Barkoulas et al., 2013)
WM118	<i>rde-1(ne300) V; nels9(nels9 [myo-3::HA::RDE-1+rol-6(su1006)]) X</i> (Watts et al., 2020)
MGH171	<i>axIs9 [vha-6p::sid-1::SL2::GFP] sid-1(qt9) V</i> (Melo and Ruvkun, 2012)
NM5179	<i>jsTi1493 [mosL loxP mex-5p FLP sl2 mNeonGreen rpl-28p FRT GFP-HIS-58 FRT3 mosR] IV</i> (Nonet, 2020)
WM45	<i>rde-1(ne300) V</i> (Tabara et al., 1999)
IG274	<i>frIs7 [nlp-29p::GFP+col-12p::DsRed] IV</i> (Pujol et al., 2008)

Other strains

Strain	Genotype
EG3200	<i>oxIs134[Pnas-37::GFP:rODC (PEST) (pWD95@90 ng/ul),lin-15(+)]</i> ; <i>lin-15(n765ts) X</i> (Davis et al., 2004; provided by D. Fay, University of Wyoming, Laramie, WY, USA)

(RMCE) (Nonet, 2020) into an *rde-1(ne300)* null mutant, generating JDW330. We used Gibson cloning to introduce a promoterless *rde-1* genomic coding sequence+3'UTR fragment into the RMCE integration vector pLF3FShC (Nonet, 2020), creating pJW2247. This vector can be linearized with AvrII+BsiWI double-digestion and promoters can be introduced by Gibson cloning (Gibson et al., 2009). We generated a *SCMp* (seam cell-specific) and *semo-1p* (hypodermis specific) by Gibson cloning of promoters into linearized pJW2247, constructing pJW2236 and pJW2264, respectively. These vectors were integrated into *jsTl1493* landing pad in JDW330 using RMCE, as described previously (Nonet, 2020). *wrt-2p* and *SCMp* promoter reporters were constructed in pJW1836 (*NLS::mScarlet::tbb-2 3' UTR*) (Ashley et al., 2021) by Gibson cloning. Plasmids were injected into N2 animals at 50 ng/μl with a pCFJ90 co-injection marker at 10 ng/μl for the *SCMp* promoter reporter and a pRF4 co-injection marker at 50 ng/μl for the *wrt-2* promoter reporter (Frøkjær-Jensen et al., 2008; Mello et al., 1991). Transgenic lines propagating extrachromosomal arrays were generated as previously described (Mello et al., 1991). Genomic and knock-in sequences are provided as GenBank-compatible .ape files on figshare.com (File S1, <https://doi.org/10.6084/m9.figshare.22270525.v1>). Sequence files for plasmids are provided as Genbank-compatible .ape files on figshare.com (File S2, <https://doi.org/10.6084/m9.figshare.22270522.v1>).

Auxin treatment

Control and auxin media/plates were made as described by Ragle et al. (2020). Control media consisted of MYOB agar+0.25% ethanol. Auxin media was made by dissolving indole 3-acetic acid (IAA; Alfa Aesar, AAA1055622) in 100% ethanol to 1.6 M and then mixing it into melted MYOB agar at 55°C to a final concentration of 4 mM before pouring plates. Control plates contained 0.25% ethanol. Temperature of the media was monitored with a Lasergrip 1080 infrared thermometer gun (Etekcity). Plates were seeded with *E. coli* OP50 and incubated overnight at room temperature. Plates were stored for up to 1 month at 4°C before use. For most auxin treatment experiments, animals were synchronized by alkaline bleaching (www.protocols.io/view/ward-lab-alkaline-bleaching-protocol-cbq9smz61). The collected eggs were incubated in M9 buffer supplemented with 5 mg/ml cholesterol at 20°C for 24 h and arrested L1 larvae were released onto the indicated type of MYOB plate. For the experiment in Table S1, a timed egg lay was performed. Twenty adult hermaphrodites animals of the indicated genotype were picked onto control (0.25% ethanol) or auxin (4 mM IAA) plates and allowed to lay eggs for 2 h. The adult animals were removed and plates were incubated for 48 h at 25°C.

Microscopy

Synchronized animals were collected from MYOB, control or auxin plates by either picking or washing off plates. For washing, 1000 μl of M9 and 0.05% gelatin was added to the plate or well, agitated to suspend animals in M9 and gelatin, and then transferred to a 1.5 ml tube. Animals were spun at 700 g for 1 min. The medium was then aspirated off and animals were resuspended in 500 μl M9 and 0.05% gelatin with 5 mM levamisole. 12 μl of animals in M9 and 0.05% levamisole solution were placed on slides with a 2% agarose pad and secured with a coverslip. For picking, animals were transferred to a 10 μl drop of M9+5 mM levamisole on a 2% agarose pad on a slide and secured with a coverslip. Images were acquired using a Plan-Apochromat 40×/1.3 Oil DIC lens, a Plan-Apochromat 63×/1.4 Oil DIC lens or a Plan-Apochromat 100×/1.4 OIL DIC lens on an AxioImager M2 microscope (Carl Zeiss Microscopy) equipped with a Colibri 7 LED light source and an Axiocam 506 mono camera. Acquired images were processed using Fiji software (version: 2.0.0-rc-69/1.52p) (Schindelin et al., 2012). For direct comparisons within a figure, we set the exposure conditions to avoid pixel saturation of the brightest sample and kept equivalent exposure for imaging of the other samples. Colocalization using a Manders' co-efficient (Manders et al., 1992, 1993) was performed as described previously (Clancy et al., 2023).

Phenotypic analysis

For the phenotypic analysis in Fig. 2, synchronized CA1200 or KRY88 larvae were released onto MYOB plates and then shifted onto control or auxin plates every 2 h up to 16 h. Animals were collected as described in the

Microscopy section and imaged by DIC microscopy to score for morphology and shedding of the L1 cuticles. For the M cell lineage experiments in Fig. S3, synchronized animals of the indicated genotypes were released onto MYOB plates and shifted onto control or auxin plates at 3 h (early shift) or 9 h (late shift) post-release and then imaged at 24 h post-release, as described in the Microscopy section. M cells were counted and recorded. For the analyses in Fig. 2E, synchronized *nhr-23::AID*, *TIR1* larvae were released on auxin plates and scored for viability and molting defects 72 h later. For the L3 shift experiments (Fig. 2F,G) synchronized animals of the indicated genotype were grown on MYOB. At 25 h post-release, they were shifted onto six-well control or auxin MYOB plates seeded with OP50. Animals were collected 23 or 72 h later, as described in the Microscopy section and imaged by DIC microscopy using a 63× lens to stage animals according to vulval morphology (Mok et al., 2015). For the reporter timecourse, synchronized *nhr-23::AID*, *TIR1*, *nas-37p::GFP::PEST* animals were released on control or auxin plates. They were then scored for GFP expression using a PlanApo 5.0×/0.5 objective on a M165 FC stereomicroscope (Leica) equipped with an X-cite FIRE LED lightsource (Excelitas) and long-pass GFP filter set (Leica, 10447407). We scored GFP expression in the head and hypodermis and did not score rectal GFP expression, as expression perdured in this tissue after head and hypodermal GFP expression ceased.

Barrier assays

Hoechst 33258 staining was performed as described previously (Moribe et al., 2004), except that we used 10 μg/ml of Hoechst 33258 as in Ward et al. (2014). Two biological replicates were performed examining 50 animals per experiment. The number of animals with either head or hypodermal nuclei staining with Hoechst 33258 were scored under a 10× DIC objective. Representative images were then taken with equivalent exposures using a 63× Oil DIC lens, as described in the imaging section. Hypo-osmotic stress sensitivity assays were performed on L4 stage larvae as described previously (Ward et al., 2014), except we used 20 μl of deionized H₂O. Each strain was assayed in triplicate.

Western blots

Animals were synchronized by alkaline bleaching, as described in the Auxin treatment section. For the blots in Figs 5B and 6B, 30 animals of the indicated genotype and stage were picked into 30 μl of M9+0.05% gelatin and 10 μl of 4×Laemmli sample buffer was added and then samples were heated at 95°C for 5 min and stored at -80°C until they were resolved by SDS-PAGE. For the blots in Fig. 6C, synchronized animals of the indicated genotype were collected at the L4 stage. Extracts of soluble cuticle proteins were prepared as described previously (Cox et al., 1981) with minor modifications. Briefly, worms were collected using M9J buffer in a 15 ml Falcon tube and washed three times with M9J buffer. Worm pellets were resuspended in 5 ml of sonication buffer and incubated on ice for 10 min and sonicated (Misonix XL-2000 Series Ultrasonic Liquid Processor, 10×10 s pulse with 10 s break) with 30 μl of 0.1 M PMSF. After sonication, samples were centrifuged at 6010 g for 2 min at 4°C and supernatants stored as fraction 1 (F1; intracellular proteins) at -20°C for the purpose of using it as loading control. Pellets were washed three times with sonication buffer and the resultant pellets were resuspended in 100 μl sonication buffer, boiled at 95°C for 2 min with 1 ml of ST buffer and incubated overnight with rotation at room temperature. After incubation, samples were centrifuged at 6010 g for 3 min and supernatants were stored as fraction 2 (F2) at -20°C. Subsequently, cuticle pellets were washed three times with 0.5% Triton X-100 and boiled at 95°C for 2 min with 300 μl of ST buffer with 5% β-mercaptoethanol and incubated with rotation at room temperature for 16 h. Finally, the samples were centrifuged at 6010 g for 3 min and supernatants collected and stored as fraction 3 (F3; soluble cuticle proteins). F3 was precipitated with methanol/chloroform and resuspended in 100 μl of rehydration buffer.

For the remaining blots, animals of the indicated genotype were washed out of wells on a six-well plate at the indicated timepoints with M9+0.05% gelatin (VWR, 97062-620), transferred to a 1.5 ml tube and washed twice more with M9+0.05% gelatin, as previously described (Vo et al., 2021). Animals were pelleted, transferred into a 100 μl volume to a new 1.5 ml tube, and flash frozen in liquid nitrogen, then stored at -80°C. Before

SDS-PAGE, samples were freeze-cracked twice in liquid nitrogen or on dry ice, Laemmli sample buffer was added to 1× and samples were heated to 95°C for 5 min. For the western blots in Fig. 1C,D, 6000 KRY88 animals per well were transferred onto a six-well MYOB plate seeded with OP50. For the western blot in Fig. 2B, 6000 synchronized KRY88 animals were plated onto control or auxin plates. Control animals were harvested at peak NHR-23 expression (12 h of growth on control plates) and auxin-treated animals were shifted onto auxin at this time; samples were taken at the indicated time points, as described above. For the western blots in Fig. S7, 500 animals of the indicated genotype were transferred into wells of a six-well control or auxin plate seeded with OP50. Animals were incubated for 24 h at 20°C and collected as described above.

For the blots in Fig. 1C,D, 10 µl of lysate and 7.5 µl of a 1:1 mix of Amersham ECL Rainbow Molecular Weight Markers (95040-114) and Precision Plus Protein Unstained Standards (1610363) was resolved by SDS-PAGE using precast 4-20% MiniProtein TGX Stain Free Gels (Bio-Rad). The blot in Fig. S7, the lysates had much more variable levels of total protein, particularly the NHR-23-depleted samples that produced an early larval arrest. Therefore, we quantified the signal of the most intense band by Stain Free imaging (Posch et al., 2013) using a Bio-Rad ChemiDoc imaging system, and ran a new gel with normalized loading. The lysates in Figs 2A, 5B, 6B and S7 were resolved as described above except we used a Spectra Multicolor Broad Range Protein Ladder (ThermoFisher Scientific, 26623). Proteins were transferred to a polyvinylidene difluoride membrane by semi-dry transfer with a TransBlot Turbo (Bio-Rad). In Figs 1C and 7C, total protein, pre- and post-transfer, was monitored using the stain-free fluorophore as described (Posch et al., 2013; Ward, 2015a). Membranes were washed in TBST and blocked in TBST+5% milk (TBST-M; Nestle Carnation Instant Nonfat Dry Milk) for 1 h at room temperature. Blots were rocked in primary antibodies in TBST-M overnight at 4°C and then washed four times for 5 min each with TBST. For primary antibodies conjugated with horseradish peroxidase (HRP), the blots were developed after the last TBST wash. Otherwise, blots were incubated with HRP-conjugated secondary antibodies in TBST-M for 1 h at room temperature followed by four 5 min TBST washes and then developed as described below. The primary antibody used for Figs 1C,D, 2A, 5B and 6B was horseradish peroxidase (HRP)-conjugated anti-FLAG M2 (Sigma-Aldrich, A8592-5x1MG, Lot #SLCB9703) at a 1:2000 dilution. Precision Protein StrepTactin-HRP Conjugate (Bio-Rad, 1610381, Lot #64426657) was included with the primary antibody at a 1:10,000 dilution to visualize the protein size standard during blot imaging for Figs 1C,D. For the blot in Figs 2A, 5B and 6B, we used mouse anti-alpha-tubulin 12G10 [Developmental Studies Hybridoma Bank, the ‘-c’ concentrated supernatant at 1:2000 (Fig. 2A, Fig. S7) or 1:4000 (Figs 5B, 6B)]. The secondary antibodies were Digital anti-mouse (Kindle Biosciences LLC, R1005) diluted 1:10,000 (Fig. 2A, Fig. S7) or 1:20,000 (Fig. S6B,C). Blots were incubated for 5 min with 1 ml of Supersignal West Femto Maximum Sensitivity Substrate (ThermoFisher Scientific, 34095) and imaged using the ‘chemi high-resolution’ setting on a Bio-Rad ChemiDoc MP System.

For the blots in Fig. 6C, 20 µl was loaded on to NuPAGE 4 to 12% protein gels with 7 µl of 4× NuPAGE LDS sample buffer as described by the manufacturer (Invitrogen, NP0322BOX) and run for 2 h at 100 V, transferred to 0.45 µm nitrocellulose membrane (Bio-Rad) at 4°C for 90 min using Bio-Rad WET transfer system. After transfer, membranes were blocked in Intercept blocking buffer (LI-COR: 927-60001) for 1 h. Later, the membrane was incubated overnight in anti-mNeonGreen primary antibody (ChromoTek, 32F6) at 1:5000 dilution at 4°C on rocker. Membranes were washed three times with TBST and incubated with secondary antibody (Sigma 12-349) at 1:100,000 dilution at room temperature on rocker for 1 h and washed three times with TBST. Blots were visualized with Supersignal West Femto detection kit (Thermo Fisher) using a LI-COR Odyssey imager. Similarly, to test the loading control, 10 µl of F1 samples were loaded and, after transfer to nitrocellulose membrane, probed with monoclonal mouse anti-actin clone C4 (ThermoFisher Scientific: ICN691001).

Bioinformatics

Fig. 3A was generated in R (R Core Team). Phase and amplitude in Table S2 were converted to x and y coordinates for each gene by calculating

$x = \text{amplitude} \times \cos(\text{phase})$ and $y = \text{amplitude} \times \sin(\text{phase})$. For Figs 3D and S5, L3 NHR-23 ChIP-Seq data was downloaded from <http://www.modencode.org> (accession ID modEncode_3837). Wig files were converted to bigwig format and loaded into the Bioconductor package SeqPlots (Huber et al., 2015; Stempor and Ahringer, 2016). A bed file with the start and end coordinates of the CDS of all genes was generated (Wormbase WS220) and loaded into SeqPlots. SeqPlots aligned all genes by the start and end position, and scaled the coding sequence of each gene to 2 kb. The average signal over all aligned genes was calculated in 25 bp windows from 1 kb upstream of the start site to 1 kb downstream of the end site. Peak calls for NHR-23 in L3 (Fig. 4C) were obtained from GEO (accession numbers: GSM1183659, GSM1183660, GSM1183661 and GSM1183666). Only peak calls validated by both replicates were considered. Peaks were assigned to the following genome features: gene body (WormBase WS220); 1 kb upstream of the start site of coding genes; between 1 kb and 3 kb upstream of the gene start site; and between 3 kb and 5 kb upstream of the gene start site. The same intervals were chosen downstream of the gene end sites. An NHR-23 peak was assigned to a feature if it overlapped with it by at least 100 bp. The peak analysis data are in Table S5. The total number of peaks in all bins was tallied and is presented in Table S2 and in Fig. 3D. For Figs 3D and 4E, the phase for the oscillating genes in Table S1 was converted to time during the molting cycle by assuming a 9 h larval stage, which makes each hour=40°. We used the phasing from Meeuse et al. (2023) with lethargus starting at 45° and ecdysis ending at 135°. The phase in hours was then plotted along the x -axis and the amplitude of the oscillating genes was plotted on the y -axis. The gene annotation was based on the Concise Description and Automated Description attributes downloaded from Wormbase.

RNAi

RNAi feeding plates were made by melting a solidified bottle of MYOB and adding carbenicillin (25 µg/ml) and IPTG (8 mM) once cooled to 55°C. dsRNA-expressing *E. coli* bacteria were streaked on LB plates with ampicillin (100 µg/ml) and grown overnight at 37°C. A single colony was picked into 25 ml LB with 100 µg/ml ampicillin and 12.5 µg/ml tetracycline and shaken overnight at 37°C at 220 RPM. The next day, the liquid culture was pelleted and resuspended in 1.25 ml LB with 100 µg/ml ampicillin, resulting in a 20× concentration from the original overnight liquid culture. 90 µl of the liquid culture was spread per small RNAi plate and allowed to dry. The plates were incubated at room temperature in the dark for 3 days. Ten adult worms from each strain were allowed to lay eggs on plates spread with *E. coli* bacteria containing either the control plasmid L4440 or the *nhr-23* RNAi knockdown plasmid for 1-2 h. The adults were removed and the eggs allowed to develop at 20°C for 2 or 3 days, depending on the experiment. For tissue-specific RNAi experiments, we used RNAi defective *rde-1* mutant animals carrying *rde-1* transgenes to rescue RNAi in specific tissues (Qadota et al., 2007). The one exception was strain MGH171, which used an intestinal-specific rescue of *sid-1* in an RNAi defective *sid-1* mutant (Melo and Ruvkun, 2012).

Statistical analysis

Statistical tests and numbers of animals analyzed are detailed in figure legends.

Acknowledgements

We thank Chris Hammell, David Matus and Julian Ceron Madrigal for their critical reading of the manuscript. We thank David Fay, Miles Puffall, Helge Grosshans and Ali Shariati for helpful discussions. We thank Jennifer Adams for generation of initial *rol-6* and *bl-1* mNeonGreen knock-ins. Some strains were provided by the Caenorhabditis Genetics Center, which is funded by the NIH Office of Research Infrastructure Programs [P40 OD010440]. L.C.J. was funded by an NIGMS training grant [T32 GM133391]. The anti-alpha tubulin 12G10 monoclonal antibody developed by J. Frankel and E.M. Nelson of the University of Iowa was obtained from the Developmental Studies Hybridoma Bank, created by the NICHD of the NIH and maintained at The University of Iowa, Department of Biology, Iowa City, IA 52242.

Competing interests

The authors declare no competing or financial interests.

Author contributions

Conceptualization: L.C.J., J.M.R., J.D.W.; Methodology: L.C.J., M.P., J.M.R., J.D.W.; Validation: L.C.J., K.M.M., M.P., J.M.R., J.D.W.; Formal analysis: L.C.J., A.A.V., J.C.C., K.M.M., M.P., J.A., M.T.L., A.R., J.M.R., A.D.C., J.D.W.; Investigation: L.C.J., A.A.V., J.C.C., K.M.M., M.P., J.A., M.T.L., C.W., A.R., J.M.R., A.D.C., J.D.W.; Resources: L.C.J., A.R., J.M.R., J.D.W.; Data curation: L.C.J., J.D.W.; Writing - original draft: L.C.J., J.D.W.; Writing - review & editing: A.A.V., J.C.C., K.M.M., M.P., J.A., M.T.L., C.W., J.M.R., A.D.C.; Visualization: L.C.J., M.P., J.A., A.R., J.M.R., J.D.W.; Supervision: J.M.R., A.D.C., J.D.W.; Project administration: J.D.W.; Funding acquisition: A.D.C., J.D.W.

Funding

This work was funded by the National Institutes of Health (NIH) National Institute of General Medical Sciences (NIGMS) (R00GM107345 and R01GM138701) and the NIH Office of the Director (R21OD033663) to J.D.W. M.P. and A.D.C. were supported by the National Institute of General Medical Sciences (R35GM134970). Open Access funding provided by the University of California. Deposited in PMC for immediate release.

Data availability

All relevant data can be found within the article and its supplementary information.

Peer review history

The peer review history is available online at <https://journals.biologists.com/dev/lookup/doi/10.1242/dev.201085.reviewer-comments.pdf>

References

- Agbulut, O., Coirault, C., Niederländer, N., Huet, A., Vicart, P., Hagège, A., Puceat, M. and Menasché, P. (2006). GFP expression in muscle cells impairs actin-myosin interactions: implications for cell therapy. *Nat. Methods* **3**, 331. doi:10.1038/nmeth0506-331
- Antebi, A. (2015). Nuclear receptor signal transduction in *C. elegans*. *WormBook*, 1-49. doi:10.1895/wormbook.1.64.2
- Ashley, G. E., Duong, T., Levenson, M. T., Martinez, M. A. Q., Johnson, L. C., Hibshman, J. D., Saeger, H. N., Palmisano, N. J., Doonan, R., Martinez-Mendez, R. et al. (2021). An expanded auxin-inducible degron toolkit for *Caenorhabditis elegans*. *Genetics* **217**, iyab006. doi:10.1093/genetics/iyab006
- Aspöck, G., Kagoshima, H., Niklaus, G. and Bürglin, T. R. (1999). *Caenorhabditis elegans* has scores of hedgehog related genes: sequence and expression analysis. *Genome Res.* **9**, 909-923. doi:10.1101/gr.9.10.909
- Baens, M., Noels, H., Broeckx, V., Hagens, S., Fevery, S., Billiau, A. D., Vankelecom, H. and Marynen, P. (2006). The dark side of EGFP: defective polyubiquitination. *PLoS ONE* **1**, e54. doi:10.1371/journal.pone.0000054
- Barkoulas, M., van Zon, J. S., Milloz, J., van Oudenaarden, A. and Félix, M.-A. (2013). Robustness and Epistasis in the *C. elegans* vulval signaling network revealed by pathway dosage modulation. *Dev. Cell* **24**, 64-75. doi:10.1016/j.devcel.2012.12.001
- Blaxter, M. L. (1993). Cuticle surface proteins of wild type and mutant *Caenorhabditis elegans*. *J. Biol. Chem.* **268**, 6600-6609. doi:10.1016/S0021-9258(18)53293-2
- Blaxter, M. L., Page, A. P., Rudin, W. and Maizels, R. M. (1992). Nematode surface coats: actively evading immunity. *Parasitol. Today* **8**, 243-247. doi:10.1016/0169-4758(92)90126-M
- Brenner, S. (1974). The genetics of *Caenorhabditis elegans*. *Genetics* **77**, 71-94. doi:10.1093/genetics/77.1.71
- Campbell, L. A., Faivre, E. J., Show, M. D., Ingraham, J. G., Flinders, J., Gross, J. D. and Ingraham, H. A. (2008). Decreased recognition of SUMO-sensitive target genes following epification of SF-1 (NR5A1). *Mol. Cell. Biol.* **28**, 7476-7486. doi:10.1128/MCB.00103-08
- Church, D. L., Guan, K. L. and Lambie, E. J. (1995). Three genes of the MAP kinase cascade, *mek-2*, *mpk-1/sur-1* and *let-60 ras*, are required for meiotic cell cycle progression in *Caenorhabditis elegans*. *Development* **121**, 2525-2535. doi:10.1242/dev.121.8.2525
- Clancy, J. C., Vo, A. A., Myles, K. M., Levenson, M. T., Ragle, J. M. and Ward, J. D. (2023). Experimental considerations for study of *C. elegans* lysosomal proteins. *G3* **13**, jkad032. doi:10.1093/g3journal/jkad032
- Clark, D. V., Suleman, D. S., Beckenbach, K. A., Gilchrist, E. J. and Baillie, D. L. (1995). Molecular cloning and characterization of the *dpy-20* gene of *Caenorhabditis elegans*. *Mol. Gen. Genet.* **247**, 367-378. doi:10.1007/BF00293205
- Cohen, J. D. and Sundaram, M. V. (2020). *C. elegans* apical extracellular matrices shape epithelia. *J. Dev. Biol.* **8**, 23. doi:10.3390/jdb8040023
- Cohen, J. D., Sparacio, A. P., Belfi, A. C., Forman-Rubinsky, R., Hall, D. H., Maul-Newby, H., Frand, A. R. and Sundaram, M. V. (2020). A multi-layered and dynamic apical extracellular matrix shapes the vulva lumen in *Caenorhabditis elegans*. *eLife* **9**, e57874. doi:10.7554/eLife.57874
- Cox, G. N., Kusch, M. and Edgar, R. S. (1981). Cuticle of *Caenorhabditis elegans*: its isolation and partial characterization. *J. Cell Biol.* **90**, 7-17. doi:10.1083/jcb.90.1.7
- Davis, M. W., Birnie, A. J., Chan, A. C., Page, A. P. and Jorgensen, E. M. (2004). A conserved metalloprotease mediates ecdysis in *Caenorhabditis elegans*. *Development* **131**, 6001-6008. doi:10.1242/dev.01454
- de Sousa Abreu, R., Penalva, L. O., Marcotte, E. M. and Vogel, C. (2009). Global signatures of protein and mRNA expression levels. *Mol. Biosyst.* **5**, 1512-1526. doi:10.1039/b908315d
- Dodd, W., Tang, L., Lone, J.-C., Wimberly, K., Wu, C.-W., Consalvo, C., Wright, J. E., Pujol, N. and Choe, K. P. (2018). A damage sensor associated with the cuticle coordinates three core environmental stress responses in *Caenorhabditis elegans*. *Genetics* **208**, 1467-1482. doi:10.1534/genetics.118.300827
- Espelt, M. V., Estevez, A. Y., Yin, X. and Strange, K. (2005). Oscillatory Ca²⁺ signaling in the isolated *Caenorhabditis elegans* intestine: role of the inositol-1,4,5-trisphosphate receptor and phospholipases C beta and gamma. *J. Gen. Physiol.* **126**, 379-392. doi:10.1085/jgp.200509355
- Fernandez, A. P., Gibbons, J. and Okkema, P. G. (2004). *C. elegans* *peb-1* mutants exhibit pleiotropic defects in molting, feeding, and morphology. *Dev. Biol.* **276**, 352-366. doi:10.1016/j.ydbio.2004.08.040
- Forman-Rubinsky, R., Cohen, J. D. and Sundaram, M. V. (2017). Lipocalins are required for apical extracellular matrix organization and remodeling in *Caenorhabditis elegans*. *Genetics* **207**, 625-642. doi:10.1534/genetics.117.300207
- Frand, A. R., Russel, S. and Ruvkun, G. (2005). Functional Genomic Analysis of *C. elegans* Molting. *PLoS Biol.* **3**, e312. doi:10.1371/journal.pbio.0030312
- Frøkjær-Jensen, C., Davis, M. W., Hopkins, C. E., Newman, B. J., Thummel, J. M., Olesen, S.-P., Grunnet, M. and Jorgensen, E. M. (2008). Single-copy insertion of transgenes in *Caenorhabditis elegans*. *Nat. Genet.* **40**, 1375-1383. doi:10.1038/ng.248
- Gerstein, M. B., Lu, Z. J., Van Nostrand, E. L., Cheng, C., Arshinoff, B. I., Liu, T., Yip, K. Y., Robilotto, R., Rechtsteiner, A., Ikegami, K. et al. (2010). Integrative analysis of the *Caenorhabditis elegans* genome by the modENCODE Project. *Science* **330**, 1775-1787. doi:10.1126/science.1196914
- Ghanta, K. S. and Mello, C. C. (2020). Melting dsDNA donor molecules greatly improves precision genome editing in *Caenorhabditis elegans*. *Genetics* **216**, 643-650. doi:10.1534/genetics.120.303564
- Ghedini, E., Wang, S., Spiro, D., Caler, E., Zhao, Q., Crabtree, J., Allen, J. E., Delcher, A. L., Guiliano, D. B., Miranda-Saavedra, D. et al. (2007). Draft genome of the filarial nematode parasite *Brugia malayi*. *Science* **317**, 1756-1760. doi:10.1126/science.1145406
- Gibson, D. G., Young, L., Chuang, R.-Y., Venter, J. C., Hutchison, C. A. and Smith, H. O. (2009). Enzymatic assembly of DNA molecules up to several hundred kilobases. *Nat. Methods* **6**, 343-345. doi:10.1038/nmeth.1318
- Gill, H. K., Cohen, J. D., Ayala-Figueroa, J., Forman-Rubinsky, R., Poggioli, C., Bickard, K., Parry, J. M., Pu, P., Hall, D. H. and Sundaram, M. V. (2016). Integrity of narrow epithelial tubes in the *C. elegans* excretory system requires a transient luminal matrix. *PLoS Genet.* **12**, e1006205. doi:10.1371/journal.pgen.1006205
- Gissendanner, C. R., Crossgrove, K., Kraus, K. A., Maina, C. V. and Sluder, A. E. (2004). Expression and function of conserved nuclear receptor genes in *Caenorhabditis elegans*. *Dev. Biol.* **266**, 399-416. doi:10.1016/j.ydbio.2003.10.014
- Guo, P., Hu, T., Zhang, J., Jiang, S. and Wang, X. (2010). Sequential action of *Caenorhabditis elegans* Rab GTPases regulates phagolysosome formation during apoptotic cell degradation. *Proc. Natl. Acad. Sci. USA* **107**, 18016-18021. doi:10.1073/pnas.1008946107
- Gupta, S. K. (2021). Human Zona Pellucida glycoproteins: binding characteristics with human spermatozoa and induction of acrosome reaction. *Front. Cell Dev. Biol.* **9**, 619868. doi:10.3389/fcell.2021.619868
- Harfe, B. D., Gomes, A. V., Kenyon, C., Liu, J., Krause, M. and Fire, A. (1998). Analysis of a *Caenorhabditis elegans* Twist homolog identifies conserved and divergent aspects of mesodermal patterning. *Genes Dev.* **12**, 2623-2635. doi:10.1101/gad.12.16.2623
- Hauser, Y. P., Meeuse, M. W. M., Gaidatzis, D. and Großhans, H. (2022). The BMP-1 transcription factor promotes oscillatory gene expression to achieve timely molting. *bioRxiv* 2021.07.05.450828.
- Hendriks, G.-J., Gaidatzis, D., Aeschmann, F. and Großhans, H. (2014). Extensive oscillatory gene expression during *C. elegans* larval development. *Mol. Cell* **53**, 380-392. doi:10.1016/j.molcel.2013.12.013
- Huber, W., Carey, V. J., Gentleman, R., Anders, S., Carlson, M., Carvalho, B. S., Bravo, H. C., Davis, S., Gatto, L., Girke, T. et al. (2015). Orchestrating high-throughput genomic analysis with Bioconductor. *Nat. Methods* **12**, 115-121. doi:10.1038/nmeth.3252
- Jetten, A. M. (2009). Retinoid-related orphan receptors (RORs): critical roles in development, immunity, circadian rhythm, and cellular metabolism. *Nucl. Recept. Signal.* **7**, e003. doi:10.1621/nrs.07003
- Johnstone, I. L. and Barry, J. D. (1996). Temporal reiteration of a precise gene expression pattern during nematode development. *EMBO J.* **15**, 3633-3639. doi:10.1002/j.1460-2075.1996.tb00732.x

- Kage-Nakadai, E., Kobuna, H., Kimura, M., Gengyo-Ando, K., Inoue, T., Arai, H. and Mitani, S. (2010). Two very long chain fatty acid acyl-CoA synthetase genes, *acs-20* and *acs-22*, have roles in the cuticle surface barrier in *Caenorhabditis elegans*. *PLoS ONE* **5**, e8857. doi:10.1371/journal.pone.0008857
- Kaletsky, R., Yao, V., Williams, A., Rannels, A. M., Tadych, A., Zhou, S., Trojanskaya, O. G. and Murphy, C. T. (2018). Transcriptome analysis of adult *Caenorhabditis elegans* cells reveals tissue-specific gene and isoform expression. *PLoS Genet.* **14**, e1007559. doi:10.1371/journal.pgen.1007559
- Kasuga, H., Fukuyama, M., Kitazawa, A., Kontani, K. and Katada, T. (2013). The microRNA miR-235 couples blast-cell quiescence to the nutritional state. *Nature* **497**, 503-506. doi:10.1038/nature12117
- Katz, S. S., Barker, T. J., Maul-Newby, H. M., Sparacio, A. P., Nguyen, K. C. Q., Maybrun, C. L., Belfi, A., Cohen, J. D., Hall, D. H., Sundaram, M. V. et al. (2022). A transient apical extracellular matrix relays cytoskeletal patterns to shape permanent acellular ridges on the surface of adult *C. elegans*. *PLoS Genet.* **18**, e1010348. doi:10.1371/journal.pgen.1010348
- Kelley, M., Yochem, J., Krieg, M., Calixto, A., Heiman, M. G., Kuzmanov, A., Meli, V., Chaffie, M., Goodman, M. B., Shaham, S. et al. (2015). FBN-1, a fibrillin-related protein, is required for resistance of the epidermis to mechanical deformation during *C. elegans* embryogenesis. *eLife* **4**, 1629. doi:10.7554/eLife.06565
- Kiefer, S. M. L. and Saling, P. (2002). Proteolytic processing of human zona pellucida proteins. *Biol. Reprod.* **66**, 407-414. doi:10.1095/biolreprod66.2.407
- Kim, D., Grün, D. and van Oudenaarden, A. (2013). Dampening of expression oscillations by synchronous regulation of a microRNA and its target. *Nat. Genet.* **45**, 1337-1344. doi:10.1038/ng.2763
- King-Jones, K. and Thummel, C. S. (2005). Nuclear receptors—a perspective from *Drosophila*. *Nat. Rev. Genet.* **6**, 311-323. doi:10.1038/nrg1581
- Kinney, B., Sahu, S., Stec, N., Hills-Muckey, K., Adams, D. W., Wang, J., Jaremko, M., Joshua-Tor, L., Keil, W. and Hammell, C. M. (2023). A circadian-like gene network regulates heterochronic miRNA transcription in *C. elegans*. *bioRxiv* 2022.09.26.509508.
- Köhnlein, K., Urban, N., Guerrero-Gómez, D., Steinbrenner, H., Urbánek, P., Priebis, J., Koch, P., Kaether, C., Miranda-Vizuete, A. and Klotz, L.-O. (2020). A *Caenorhabditis elegans* ortholog of human selenium-binding protein 1 is a pro-aging factor protecting against selenite toxicity. *Redox Biol.* **28**, 101323. doi:10.1016/j.redox.2019.101323
- Kostrouchova, M., Krause, M., Kostrouch, Z. and Rall, J. E. (1998). CHR3: a *Caenorhabditis elegans* orphan nuclear hormone receptor required for proper epidermal development and molting. *Development* **125**, 1617-1626. doi:10.1242/dev.125.9.1617
- Kostrouchova, M., Krause, M., Kostrouch, Z. and Rall, J. E. (2001). Nuclear hormone receptor CHR3 is a critical regulator of all four larval molts of the nematode *Caenorhabditis elegans*. *Proc. Natl. Acad. Sci. USA* **98**, 7360-7365. doi:10.1073/pnas.131171898
- Kouns, N. A., Nakielna, J., Behensky, F., Krause, M. W., Kostrouch, Z. and Kostrouchova, M. (2011). NHR-23 dependent collagen and hedgehog-related genes required for molting. *Biochem. Biophys. Res. Commun.* **413**, 515-520. doi:10.1016/j.bbrc.2011.08.124
- Kramer, J. M. and Johnson, J. J. (1993). Analysis of mutations in the *sqt-1* and *rol-6* collagen genes of *Caenorhabditis elegans*. *Genetics* **135**, 1035-1045. doi:10.1093/genetics/135.4.1035
- Lam, G. T., Jiang, C. and Thummel, C. S. (1997). Coordination of larval and prepupal gene expression by the DHR3 orphan receptor during *Drosophila* metamorphosis. *Development* **124**, 1757-1769. doi:10.1242/dev.124.9.1757
- Lažetić, V. and Fay, D. S. (2017). Molting in *C. elegans*. *Worm* **6**, e1330246. doi:10.1080/21624054.2017.1330246
- Lin, K., Dorman, J. B., Rodan, A. and Kenyon, C. (1997). *daf-16*: an HNF-3/ forkhead family member that can function to double the life-span of *Caenorhabditis elegans*. *Science* **278**, 1319-1322. doi:10.1126/science.278.5341.1319
- Macneil, L. T., Watson, E., Arda, H. E., Zhu, L. J. and Walhout, A. J. M. (2013). Diet-induced developmental acceleration independent of TOR and insulin in *C. elegans*. *Cell* **153**, 240-252. doi:10.1016/j.cell.2013.02.049
- Manders, E. M., Stap, J., Brakenhoff, G. J., van Driel, R. and Aten, J. A. (1992). Dynamics of three-dimensional replication patterns during the S-phase, analysed by double labelling of DNA and confocal microscopy. *J. Cell Sci.* **103**, 857-862. doi:10.1242/jcs.103.3.857
- Manders, E. M. M., Verbeek, F. J. and Aten, J. A. (1993). Measurement of co-localization of objects in dual-colour confocal images. *J. Microsc.* **169**, 375-382. doi:10.1111/j.1365-2818.1993.tb03313.x
- Meewe, M. W. M., Hauser, Y. P., Morales Moya, L. J., Hendriks, G. J., Eglinger, J., Bogaarts, G., Tsiairis, C. and Großhans, H. (2020). Developmental function and state transitions of a gene expression oscillator in *Caenorhabditis elegans*. *Mol. Syst. Biol.* **16**, e9975. doi:10.15252/msb.20209498
- Meewe, M. W. M., Hauser, Y. P., Nahar, S., Smith, A. A. T., Braun, K., Azzi, C., Rempfler, M. and Großhans, H. (2023). *C. elegans* molting requires rhythmic accumulation of the Grainyhead/LSF transcription factor GRH-1. *EMBO J.* **42**, e111895. doi:10.15252/embj.2022111895
- Mello, C. C., Kramer, J. M., Stinchcomb, D. and Ambros, V. (1991). Efficient gene transfer in *C. elegans*: extrachromosomal maintenance and integration of transforming sequences. *EMBO J.* **10**, 3959-3970. doi:10.1002/j.1460-2075.1991.tb04966.x
- Melo, J. A. and Ruvkun, G. (2012). Inactivation of conserved *C. elegans* genes engages pathogen- and xenobiotic-associated defenses. *Cell* **149**, 452-466. doi:10.1016/j.cell.2012.02.050
- Mok, D. Z. L., Sternberg, P. W. and Inoue, T. (2015). Morphologically defined sub-stages of *C. elegans* vulval development in the fourth larval stage. *BMC Dev. Biol.* **15**, 26. doi:10.1186/s12861-015-0076-7
- Moribe, H., Yochem, J., Yamada, H., Tabuse, Y., Fujimoto, T. and Mekada, E. (2004). Tetraspanin protein (TSP-15) is required for epidermal integrity in *Caenorhabditis elegans*. *J. Cell Sci.* **117**, 5209-5220. doi:10.1242/jcs.01403
- Nelson, F. K., Albert, P. S. and Riddle, D. L. (1983). Fine structure of the *Caenorhabditis elegans* secretory-excretory system. *J. Ultrastruct. Res.* **82**, 156-171. doi:10.1016/S0022-5320(83)90050-3
- Nonet, M. L. (2020). Efficient transgenesis in *Caenorhabditis elegans* using Flp recombinase-mediated cassette exchange. *Genetics* **215**, 903-921. doi:10.1534/genetics.120.303388
- Page, A. P. and Johnstone, I. L. (2007). The cuticle. *WormBook*, 1-15. doi:10.1895/wormbook.1.138
- Paix, A., Wang, Y., Smith, H. E., Lee, C.-Y. S., Calidas, D., Lu, T., Smith, J., Schmidt, H., Krause, M. W. and Seydoux, G. (2014). Scalable and versatile genome editing using linear DNAs with microhomology to Cas9 sites in *Caenorhabditis elegans*. *Genetics* **198**, 1347-1356. doi:10.1534/genetics.114.170423
- Paix, A., Folkmann, A., Rasoloson, D. and Seydoux, G. (2015). High efficiency, homology-directed genome editing in *Caenorhabditis elegans* using CRISPR-Cas9 Ribonucleoprotein complexes. *Genetics* **201**, 47-54. doi:10.1534/genetics.115.179382
- Patel, R., Galagali, H., Kim, J. K. and Frand, A. R. (2022). Feedback between a retinoid-related nuclear receptor and the *let-7* microRNAs controls the pace and number of molting cycles in *C. elegans*. *eLife* **11**, e80010. doi:10.7554/eLife.80010
- Posch, A., Kohn, J., Oh, K., Hammond, M. and Liu, N. (2013). V3 stain-free workflow for a practical, convenient, and reliable total protein loading control in western blotting. *J. Vis. Exp.* **82**, 50948. doi:10.3791/50948
- Pujol, N., Cypowyj, S., Ziegler, K., Millet, A., Astrain, A., Goncharov, A., Jin, Y., Chisholm, A. D. and Ewbank, J. J. (2008). Distinct innate immune responses to infection and wounding in the *C. elegans* epidermis. *Curr. Biol.* **18**, 481-489. doi:10.1016/j.cub.2008.02.079
- Qadota, H., Inoue, M., Hikita, T., Köppen, M., Hardin, J. D., Amano, M., Moerman, D. G. and Kaibuchi, K. (2007). Establishment of a tissue-specific RNAi system in *C. elegans*. *Gene* **400**, 166-173. doi:10.1016/j.gene.2007.06.020
- R Core Team (2007). *R: A language and environment for statistical computing*. R Foundation for Statistical Computing, Vienna, Austria. <https://www.R-project.org/>
- Ragle, J. M., Aita, A. L., Morrison, K. N., Martinez-Mendez, R., Saeger, H. N., Ashley, G. A., Johnson, L. C., Schubert, K. A., Shakes, D. C. and Ward, J. D. (2020). The conserved molting/circadian rhythm regulator NHR-23/NR1F1 serves as an essential co-regulator of *C. elegans* spermatogenesis. *Development* **147**, dev193862. doi:10.1242/dev.193862
- Ragle, J. M., Morrison, K. N., Vo, A. A., Johnson, Z. E., Hernandez Lopez, J., Rechtsteiner, A., Shakes, D. C. and Ward, J. D. (2022). NHR-23 and SPE-44 regulate distinct sets of genes during *C. elegans* spermatogenesis. *G3* **12**, jkac256. doi:10.1093/g3journal/jkac256
- Ruaud, A.-F. and Bessereau, J.-L. (2006). Activation of nicotinic receptors uncouples a developmental timer from the molting timer in *C. elegans*. *Development* **133**, 2211-2222. doi:10.1242/dev.02392
- Ruaud, A.-F., Lam, G. and Thummel, C. S. (2010). The *Drosophila* nuclear receptors DHR3 and β FTZ-F1 control overlapping developmental responses in late embryos. *Development* **137**, 123-131. doi:10.1242/dev.042036
- Sandhu, A., Badal, D., Sheokand, R., Tyagi, S. and Singh, V. (2021). Specific collagens maintain the cuticle permeability barrier in *Caenorhabditis elegans*. *Genetics* **217**, iyaa047. doi:10.1093/genetics/iyaa047
- Sapio, M. R., Hilliard, M. A., Cermola, M., Favre, R. and Bazzicalupo, P. (2005). The Zona Pellucida domain containing proteins, CUT-1, CUT-3 and CUT-5, play essential roles in the development of the larval alae in *Caenorhabditis elegans*. *Dev. Biol.* **282**, 231-245. doi:10.1016/j.ydbio.2005.03.011
- Schindelin, J., Arganda-Carreras, I., Frise, E., Kaynig, V., Longair, M., Pietzsch, T., Preibisch, S., Rueden, C., Saalfeld, S., Schmid, B. et al. (2012). Fiji: an open-source platform for biological-image analysis. *Nat. Methods* **9**, 676-682. doi:10.1038/nmeth.2019
- Singh, R. N. and Sulston, J. E. (1978). Some observations on molting in *C. elegans*. *Nematologica* **24**, 63-71. doi:10.1163/187529278X000074
- Stec, N., Doerfel, K., Hills-Muckey, K., Etorre, V. M., Ercan, S., Keil, W. and Hammell, C. M. (2021). An epigenetic priming mechanism mediated by nutrient sensing regulates transcriptional output during *C. elegans* development. *Curr. Biol.* **31**, 809-826.e6. doi:10.1016/j.cub.2020.11.060

- Stempor, P. and Ahringer, J.** (2016). SeqPlots - Interactive software for exploratory data analyses, pattern discovery and visualization in genomics. *Wellcome Open Res.* **1**, 14. doi:10.12688/wellcomeopenres.10004.1
- Stojanovski, K., Großhans, H. and Towbin, B. D.** (2022). Coupling of growth rate and developmental tempo reduces body size heterogeneity in *C. elegans*. *Nat. Commun.* **13**, 3132. doi:10.1038/s41467-022-29720-8
- Sulston, J. E. and Horvitz, H. R.** (1977). Post-embryonic cell lineages of the nematode, *Caenorhabditis elegans*. *Dev. Biol.* **56**, 110-156. doi:10.1016/0012-1606(77)90158-0
- Tabara, H., Sarkissian, M., Kelly, W. G., Fleenor, J., Grishok, A., Timmons, L., Fire, A. and Mello, C. C.** (1999). The *rde-1* gene, RNA interference, and transposon silencing in *C. elegans*. *Cell* **99**, 123-132. doi:10.1016/S0092-8674(00)81644-X
- Taubert, S., Ward, J. D. and Yamamoto, K. R.** (2011). Nuclear hormone receptors in nematodes: Evolution and function. *Mol. Cell. Endocrinol.* **334**, 49-55. doi:10.1016/j.mce.2010.04.021
- Telford, M. J., Bourlat, S. J., Economou, A., Papillon, D. and Rota-Stabelli, O.** (2008). The evolution of the Ecdysozoa. *Philos. Trans. R. Soc. B Biol. Sci.* **363**, 1529-1537. doi:10.1098/rstb.2007.2243
- Teuscher, A. C., Jongsma, E., Davis, M. N., Statzer, C., Gebauer, J. M., Naba, A. and Ewald, C. Y.** (2019). The *in-silico* characterization of the *Caenorhabditis elegans* matrisome and proposal of a novel collagen classification. *Matrix Biol. Plus* **1**, 100001. doi:10.1016/j.mbplus.2018.11.001
- Tong, A., Lynn, G., Ngo, V., Wong, D., Moseley, S. L., Ewbank, J. J., Goncharov, A., Wu, Y.-C., Pujol, N. and Chisholm, A. D.** (2009). Negative regulation of *Caenorhabditis elegans* epidermal damage responses by death-associated protein kinase. *Proc. Natl. Acad. Sci. USA* **106**, 1457-1461. doi:10.1073/pnas.0809339106
- Tsiairis, C. and Großhans, H.** (2021). Chapter Two - Gene expression oscillations in *C. elegans* underlie a new developmental clock. In *Current Topics in Developmental Biology* (ed. S. Jarriault and B. Podbilewicz), pp. 19-43. Academic Press.
- Vo, A. A., Levenson, M. T., Ragle, J. M. and Ward, J. D.** (2021). Efficient generation of a single-copy *eft-3p::TIR1::F2A::BFP::AID*::NLS* allele in the *C. elegans* *ttTI5605* insertion site through recombination-mediated cassette exchange. *MicroPublication Biol.* **2021**, 10.17912/micropub.biology.000425.
- Vogel, C. and Marcotte, E. M.** (2012). Insights into the regulation of protein abundance from proteomic and transcriptomic analyses. *Nat. Rev. Genet.* **13**, 227-232. doi:10.1038/nrg3185
- Vuong-Breder, T. T. K., Suman, S. K. and Labouesse, M.** (2017). The apical ECM preserves embryonic integrity and distributes mechanical stress during morphogenesis. *Development* **144**, 4336-4349. doi:10.1242/dev.150383
- Ward, J. D.** (2015a). Rapid and precise engineering of the *Caenorhabditis elegans* genome with lethal mutation co-conversion and inactivation of NHEJ repair. *Genetics* **199**, 363-377. doi:10.1534/genetics.114.172361
- Ward, J. D.** (2015b). Rendering the intractable more tractable: tools from *Caenorhabditis elegans* ripe for import into parasitic nematodes. *Genetics* **201**, 1279-1294. doi:10.1534/genetics.115.182717
- Ward, J. D., Bojanala, N., Bernal, T., Ashrafi, K., Asahina, M. and Yamamoto, K. R.** (2013). Sumoylated NHR-25/NR5A regulates cell fate during *C. elegans* vulval development. *PLoS Genet.* **9**, e1003992. doi:10.1371/journal.pgen.1003992
- Ward, J. D., Mullaney, B., Schiller, B. J., He, L. D., Petnic, S. E., Couillault, C., Pujol, N., Bernal, T. U., Van Gilst, M. R., Ashrafi, K. et al.** (2014). Defects in the *C. elegans* acyl-CoA synthase, *acs-3*, and nuclear hormone receptor, *nhr-25*, cause sensitivity to distinct, but overlapping stresses. *PLoS ONE* **9**, e92552. doi:10.1371/journal.pone.0092552
- Watts, J. S., Harrison, H. F., Omi, S., Guenthers, Q., Dalelio, J., Pujol, N. and Watts, J. L.** (2020). New strains for tissue-specific RNAi studies in *Caenorhabditis elegans*. *G3* **10**, 4167-4176. doi:10.1534/g3.120.401749
- Zaslavler, A., Mayo, A. E., Rosenberg, R., Bashkin, P., Sberro, H., Tsalyuk, M., Surette, M. G. and Alon, U.** (2004). Just-in-time transcription program in metabolic pathways. *Nat. Genet.* **36**, 486-491. doi:10.1038/ng1348
- Zhang, C. and Ruvkun, G.** (2012). New insights into siRNA amplification and RNAi. *RNA Biol.* **9**, 1045-1049. doi:10.4161/ma.21246
- Zhang, L., Ward, J. D., Cheng, Z. and Dernburg, A. F.** (2015). The auxin-inducible degradation (AID) system enables versatile conditional protein depletion in *C. elegans*. *Development* **142**, 4374-4384. doi:10.1242/dev.129635
- Zugasti, O. and Ewbank, J. J.** (2009). Neuroimmune regulation of antimicrobial peptide expression by a noncanonical TGF- β signaling pathway in *Caenorhabditis elegans* epidermis. *Nat. Immunol.* **10**, 249-256. doi:10.1038/ni.1700

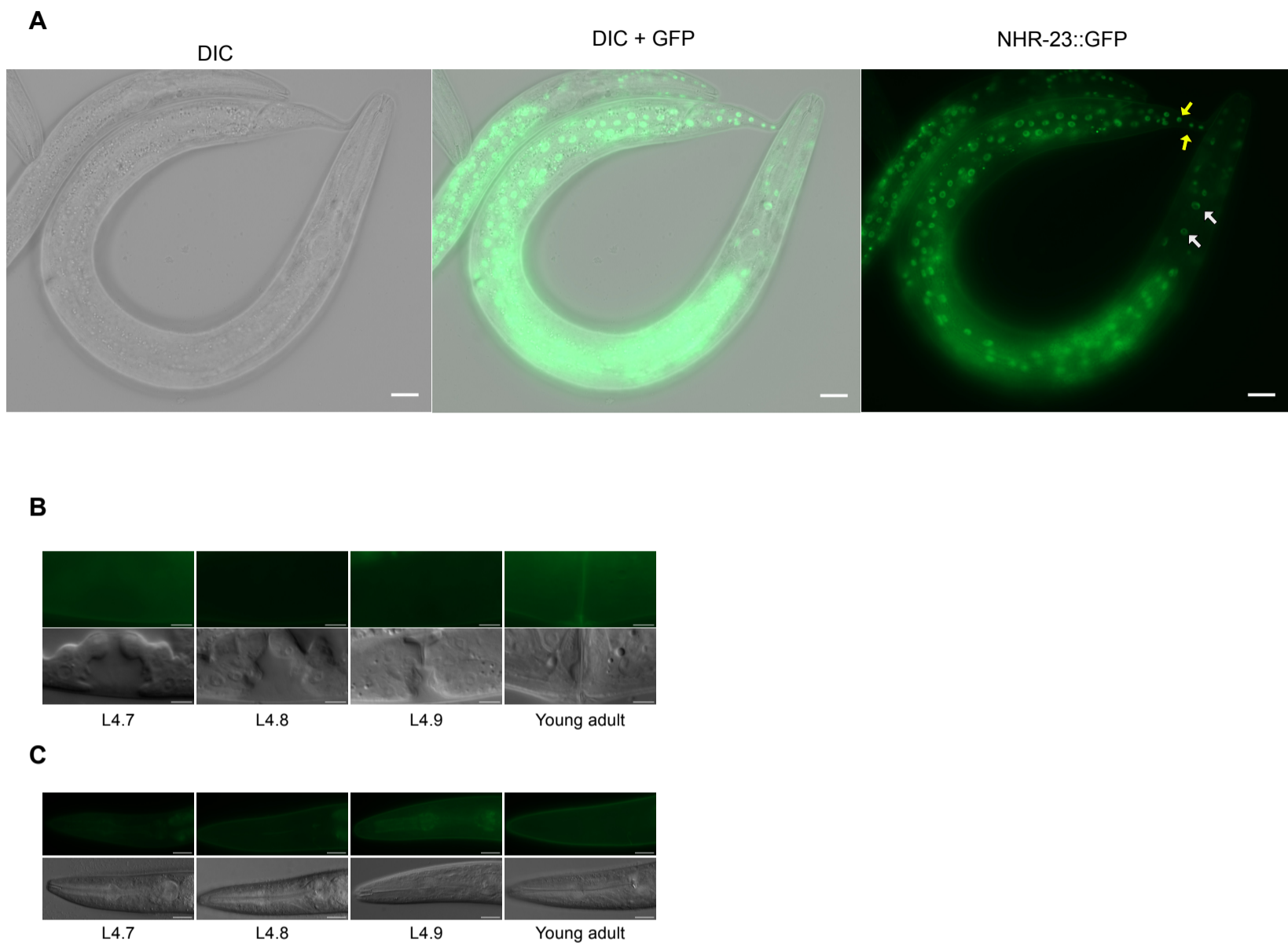


Fig. S1. NHR-23::GFP expression. (A) Representative image of NHR-23 expression in *nhr-23::GFP::AID*::3xFLAG; TIR-1* L4 animals. NHR-23 expression is seen in the hypodermis and developing germline, as described in Ragle et al. 2020. White arrows point to seam cells expressing GFP and yellow arrows point to hyp cells expressing GFP. NHR-23 expression in the vulva (B) and head (C) of *nhr-23::GFP::AID*::3xFLAG* animals of the indicated stages. Images are representative of 20 animals examined over 4 independent experiments. Scale bars=5 μ m (B) or 20 μ m (C). Animals were staged based on vulval morphology (Mok et al., 2015).

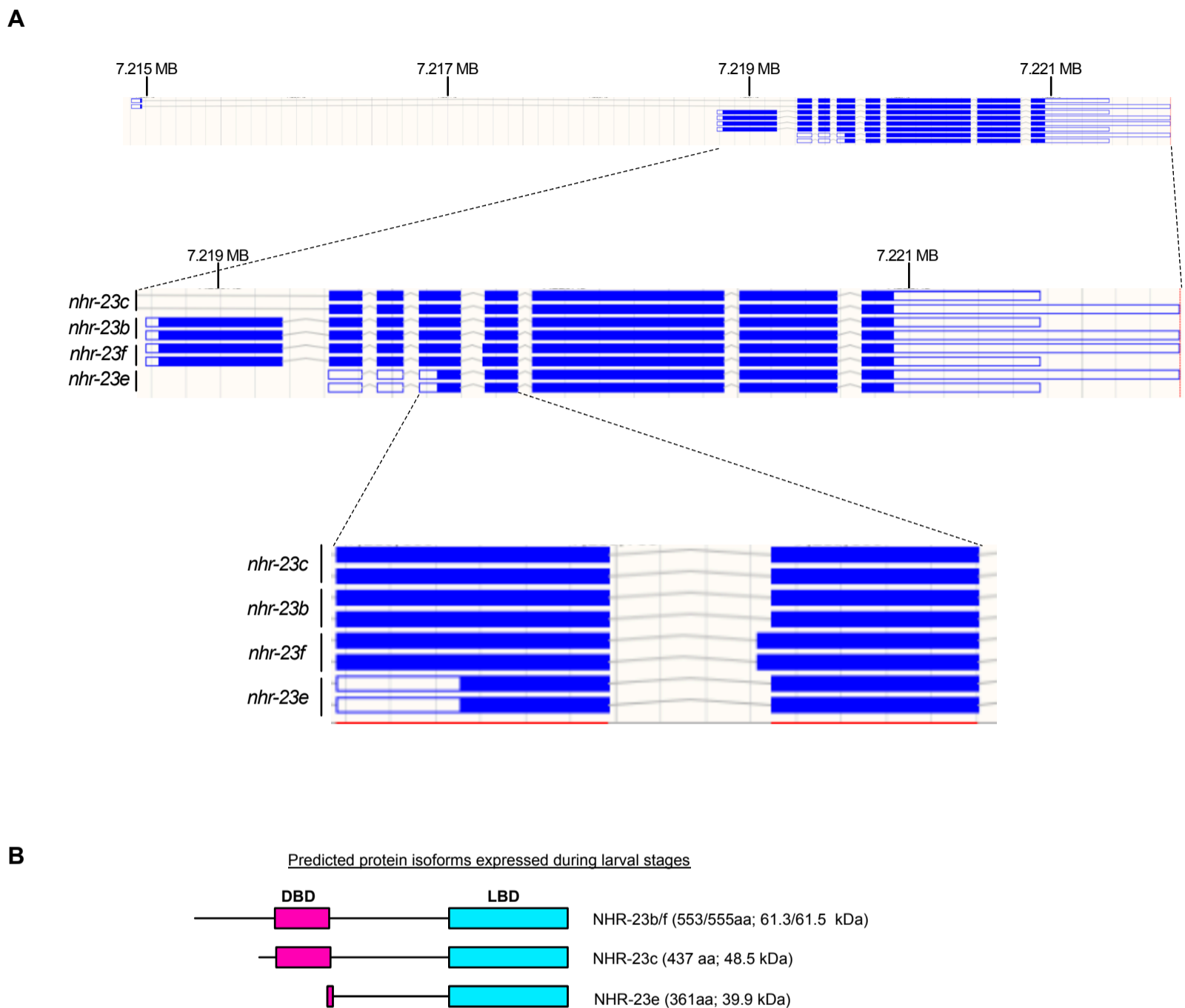


Fig. S2. *nhr-23* isoforms detected by Nanopore direct mRNA sequencing. (A) Gene model diagrams of the *nhr-23* isoforms from the “observed isoforms” track on the ENSEMBL genome track. These are isoforms confirmed by direct mRNA sequencing (Roach et al., 2020). The top tracks are of the full *nhr-23* gene, including the *nhr-23c* isoforms, which contain a large first intron. The middle tracks are a zoomed in view starting at the *nhr-23b* transcription start site. The bottom tracks are further zoomed in to depict the alternative 3’ splice site usage that generates *nhr-23b* and *nhr-23f*. (B) Cartoons of predicted protein isoforms expressed during larval development based on Nanopore direct mRNA sequencing data (Roach et al., 2020). All of the predicted isoforms contain a Ligand Binding Domain (LBD) while only two of the three have a DNA Binding Domain (DBD). The predicted size of each isoform is listed to the right of the structure in amino acids (aa) and kDa. The AID*::3xFLAG fusion is predicted to add 9 kDa.

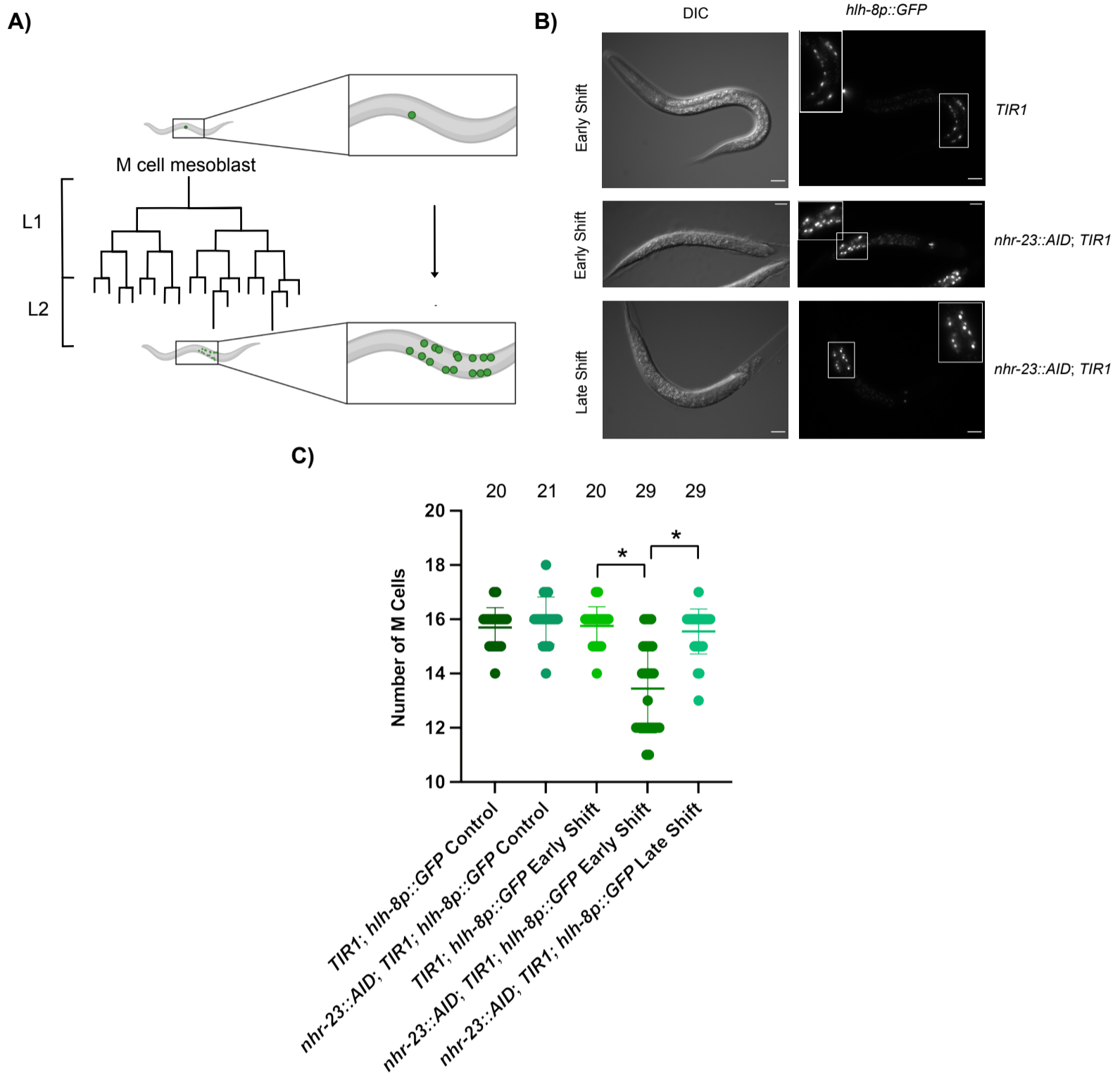


Fig. S3. NHR-23 depletion causes developmental delay (A) Depiction of the M cell mesoblast cell divisions in L1 larvae created with BioRender.com. Newly hatched animals are born with a single M cell, which undergoes the indicated set of divisions to produce 16 descendent cells at the L1/L2 molt. An *hlh-8p::GFP* reporter can be used to monitor M cell divisions in living animals. (B and C) Animals of the indicated genotype were synchronized and shifted to either auxin or control plates at either 3 (early shift) or 9 hours (late shift) post-release and imaged at 24 hours post-release. Two biological replicates were performed. (B) Representative images of animals of the indicated genotypes on auxin plates. (C) M cell quantification for animals of the indicated genotype shifted to control or auxin plates. Mean and standard deviation are labeled. The number of animals assayed for each genotype and condition is indicated at the top of the graph (* two-tailed T-test $p < 0.0001$).

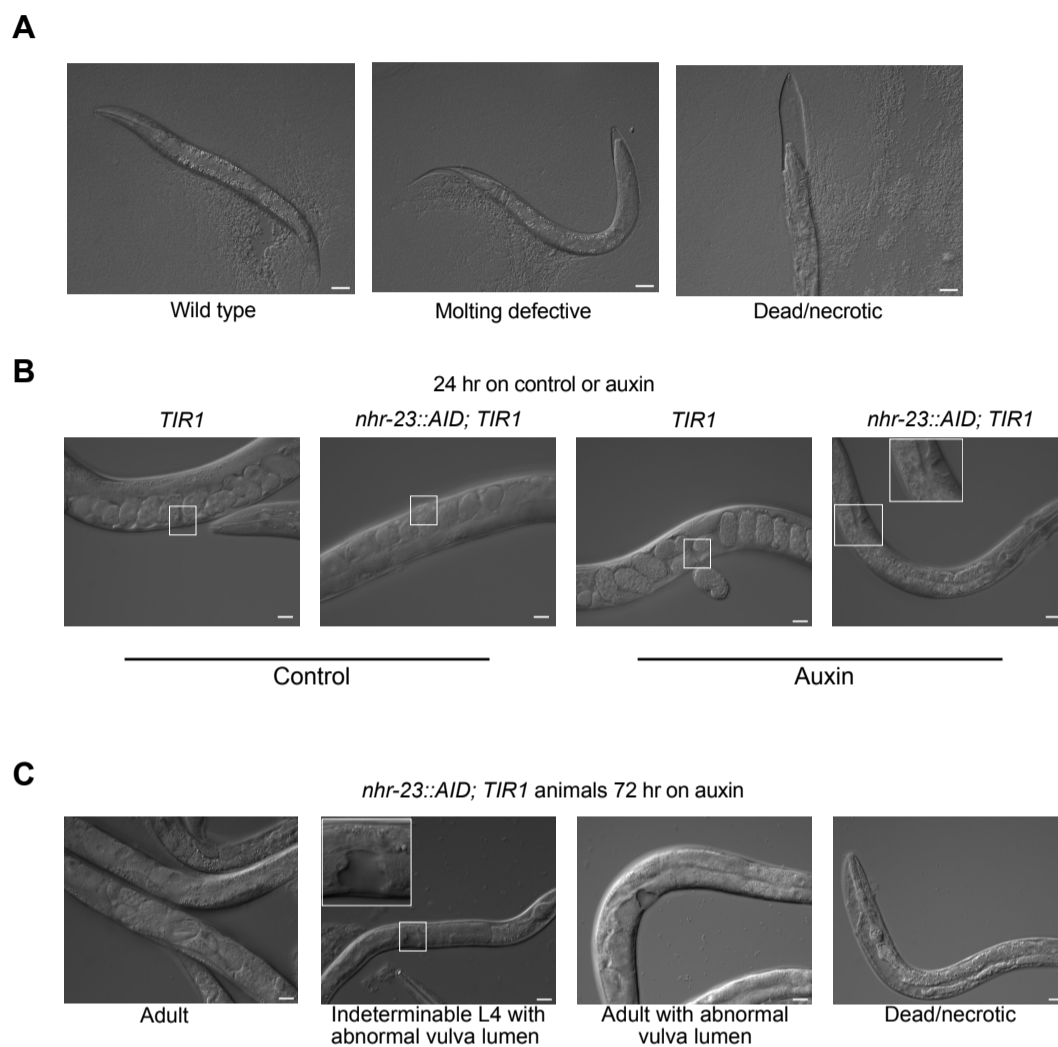


Fig. S4. NHR-23 depletion causes developmental delay. (A) Representative images of synchronized *nhr-23::AID; TIR1* L1 larvae released on auxin and scored for molting defects and death/necrosis 72 hours post-release. (B) Representative images of animals of the indicated genotype that were synchronized and shifted onto auxin at 25 hours post-release and imaged 23 hours later (48 hours post-release). The position of the vulva is highlighted with a white box. (C) Representative images of *nhr-23::AID; TIR1* animals treated as in (B) and scored after 72 hours on auxin. Scale bars=20 μ m. A zoomed inset is provided for the auxin-treated *nhr-23::AID, TIR1* images in B and C to highlight vulval morphology.

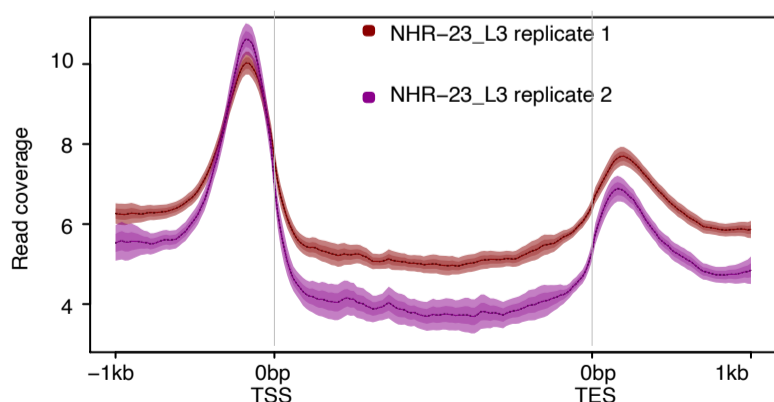


Fig. S5. NHR-23 enrichment around genes. Average signal over all aligned genes from two NHR-23 ChIP-seq replicates (Gerstein et al., 2010). The y-axis indicates non-normalized read coverage. The mean signal is plotted with a line and the mean's 95% confidence interval is indicated by the shaded area. TSS=transcription start site; TES=transcription end site.

A

Strain	Genotype	Brood size (\pm std. dev.)
N2	Wild type	290 \pm 48
JDW459	<i>nhr-23::AID; TIR1, rol-6::mNG::3xFLAG</i>	293 \pm 48
JDW463	<i>nhr-23::AID; TIR1, bli-1::mNG::3xFLAG(int)</i>	236 \pm 56
JDW475	<i>noah-1::mNG::3xFLAG(int), nhr-23::AID; TIR1</i>	246 \pm 27

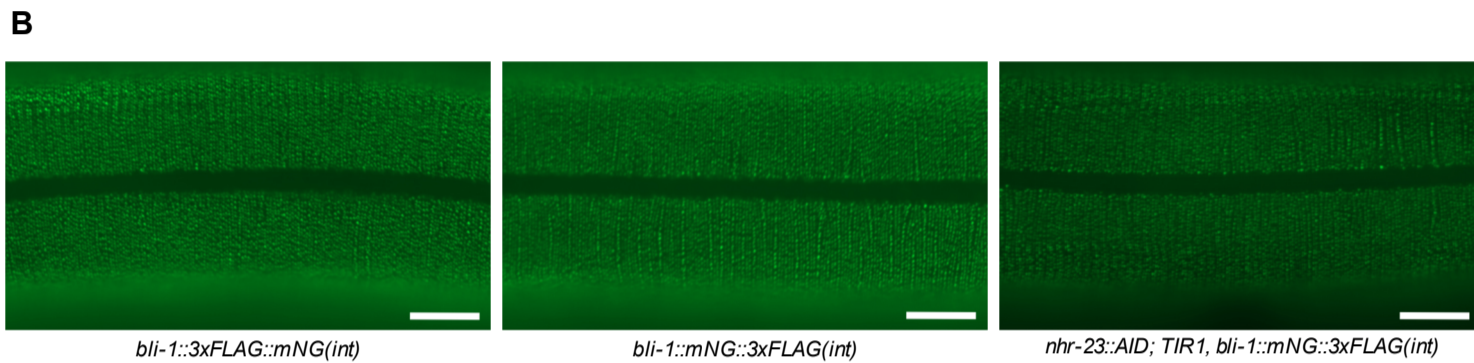


Fig. S6. Validation of *bli-1*, *noah-1*, and *rol-6* knock-in strains. (A) Brood size analysis of animals of the indicated genotype. (B) Representative images from L4.9 stage CZ27591 *bli-1(ju1789[bli-1::3xFLAG::mNG(int)]) II*, JDW389 *bli-1(wrd84[bli-1::mNG::3xFLAG(int)]) II*, and JDW463 *nhr-23(kry61(nhr-23::AID*-TEV-3xFLAG)) I; ieSi57 [Peft-3::TIR1::mRuby::unc-54 3'UTR, cb-unc-119(+)]*, *bli-1(wrd84[bli-1::mNG::3xFLAG(int)])* animals. Equal 500 msec exposures from the same area of animals were taken using a 100x objective. Knock-ins are all at the same location in *bli-1* (see Fig. 6A). Scale bars=10 μ m. Images are representative of 40 animals examined in two independent experiments.

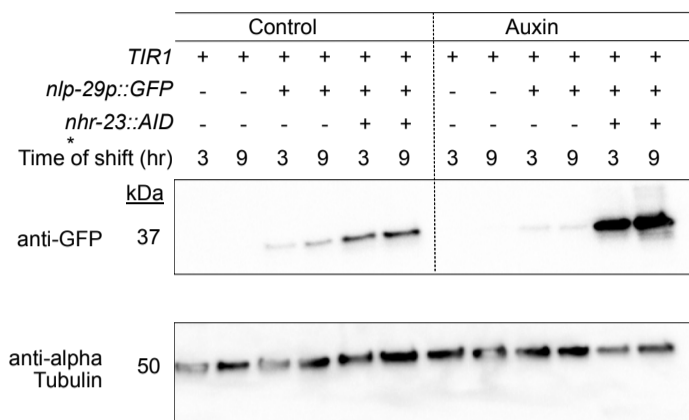


Fig. S7. Depletion of NHR-23 leads to an elevated *nlp-29p::GFP* reporter activity. Anti-GFP immunoblot analysis of *nlp-29p::GFP* expression. Marker size (in kDa) is provided. An anti-tubulin immunoblot is provided as a loading control. The blots are representative of two experimental replicates.

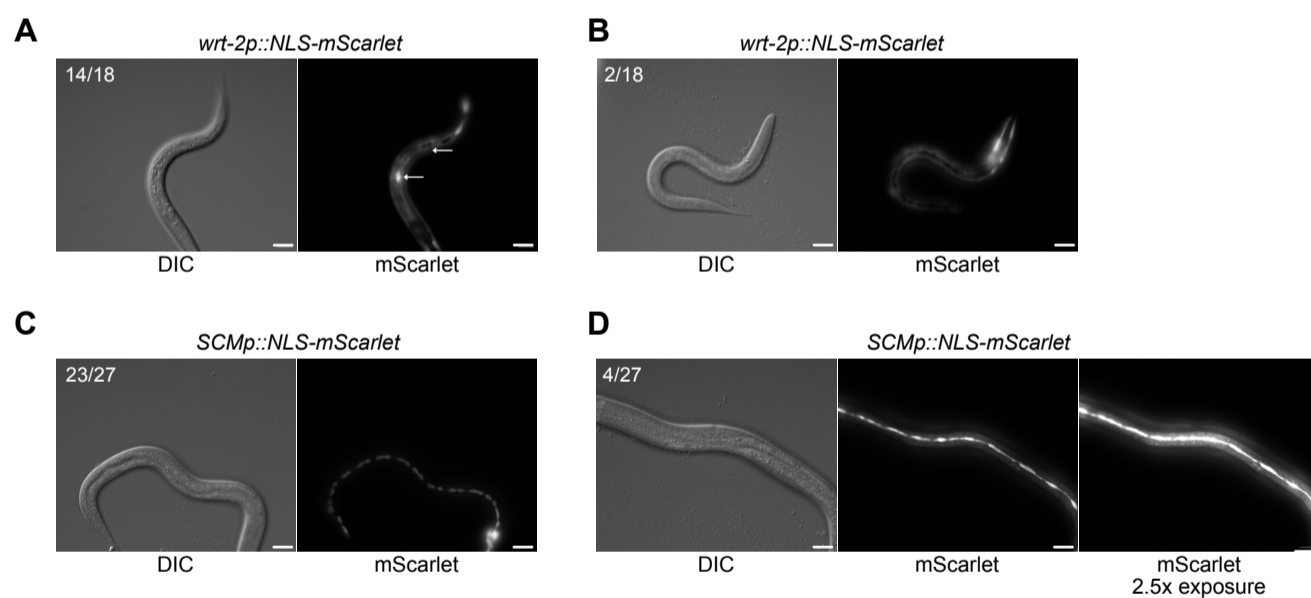


Fig. S8. Expression patterns of *SCMp* and *wrt-2* promoter reporters. *wrt-2p::NLS::mScarlet* is expressed in the hypodermis and seam cells (A and B). In some animals seam cell expression is lacking. In A, arrows point to two seam cells, one with reporter expression and one lacking it. *SCMp::NLS::mScarlet* promoter reporters express robustly in the seam cells (C) with weak expression in the hypodermis (D) in a subset of animals. Two biological replicates were performed and the number of animals for which each image is representative is indicated.

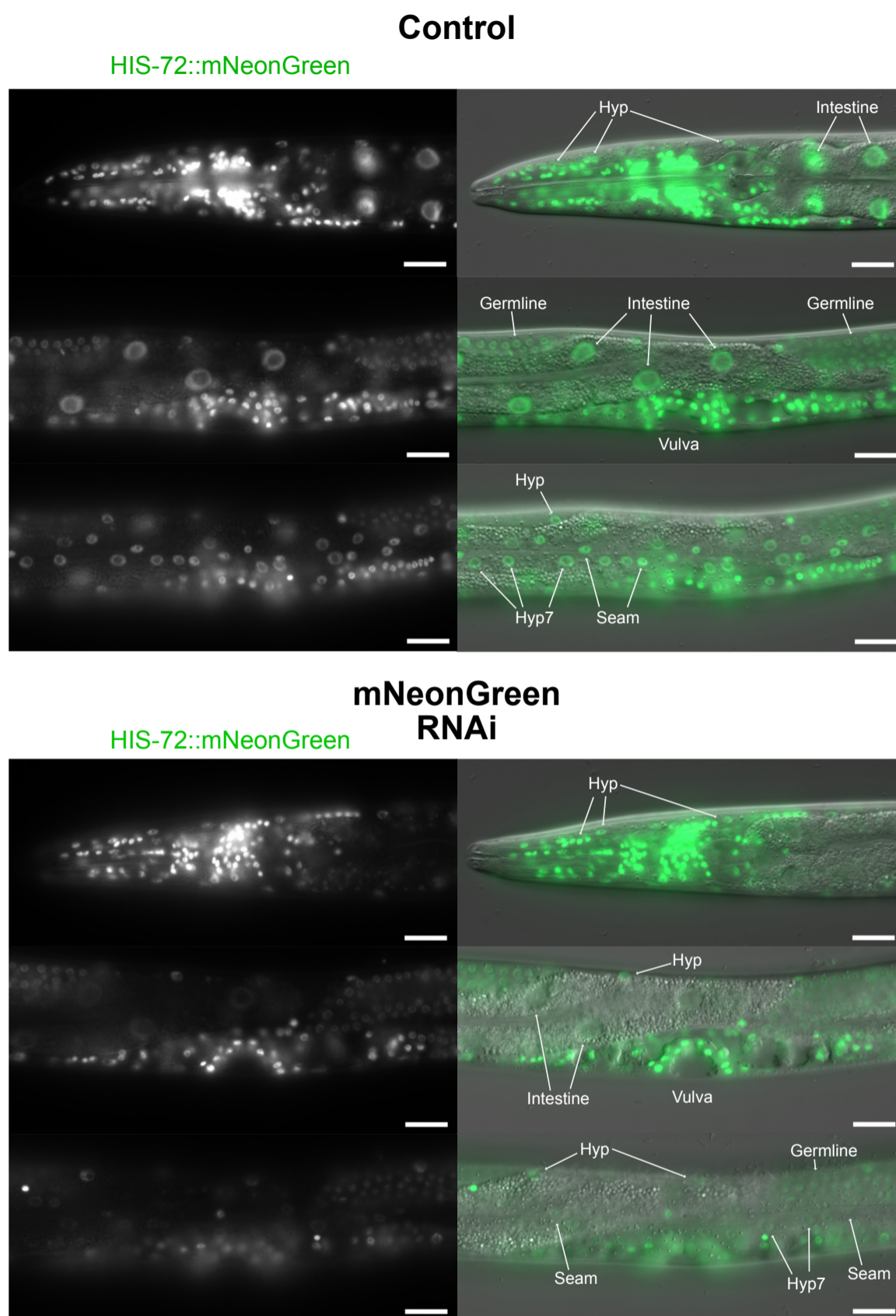


Fig. S9. JDW525 animals are permissive for RNAi knockdown in seam, hypodermal, and intestinal cells. JDW 525 [*his-72(wrd142[mNeonGreen::his-72]) III ; jsTi1493 {mosL loxP [wrdSi65(SCMp::rde-1 CDS +3'UTR)] FRT3::mosR} IV ; rde-1 (ne300) V*] animals grown on control RNAi display HIS-72::mNG expression in hypodermal, intestinal, germline, vulval, and seam cells. mNeonGreen RNAi caused reduction of HIS-72::mNG expression in seam, intestinal, and syncytial hypodermal (*hyp7*) cells. Vulval, germline, and head hypodermal expression was unaffected. Scale bars=20µm. Data are representative of forty animals examined over two biological replicates

Table S1. *TIR1*, *nhr-23::GFP::AID*::3xFLAG* has milder developmental delay than *TIR1*, *nhr-23::AID*::3xFLAG* on auxin

Genotype	Treatment	N	% Developmental delay
<i>TIR1; nhr-23::AID*::3xFLAG</i>	Control	296	0.34
	Auxin	237	100.00
<i>TIR1; nhr-23::GFP::AID*::3xFLAG</i>	Control	259	0.39
	Auxin	257	7.62

Animals were synchronized by a timed egg lay. Percent developmental delay is the number of animals that failed to reach L4 after 48 hours at 25°C divided by the total number of animals scored, multiplied by 100%.

Table S2. *nhr-23*-regulated oscillating and non-oscillating genes

[Click here to download Table S2](#)

Table S3. Gene ontology analysis of NHR-23-regulated oscillating genes

Gene Ontology (GO) term	Description	Enrichment	q-value
GO:0042302	structural constituent of cuticle	7.54	2.23E-07
GO:0042329	structural constituent of collagen and cuticulin-based cuticle	31.06	1.80E-05
GO:0005198	structural molecule activity	3.21	6.33E-03
GO:0004867	serine-type endopeptidase inhibitor activity	5.73	3.97E-01
GO:0008237	metallopeptidase activity	3.78	3.37E-01

Enrichment: observed/expected occurrence of a GO term in the *nhr-23*-regulated gene set
q value: p value adjusted for false discovery rate

Table S4. Gene ontology analysis of all oscillating genes

[Click here to download Table S4](#)

Table S5. NHR-23 ChIP-seq peaks broken down by position relative to coding sequence.

[Click here to download Table S5](#)

Table S6. crRNAs used for this study

Number	Target	crRNA sequence (5'-3', PAM not included)
1	<i>his-72</i> N-terminus	GGTACGAGCCATTGTTGTTTC
51	<i>noah-1</i> internal	GTTGAGTGTGCTTTAACCGG
318	<i>bli-1</i> internal knock-in	AGATTCATCTTCTGCAGCTT
351	<i>rol-6</i> C-terminus	GTCATGAATTTGTCTACAAT

Table S7. PCR primers used for knock-ins and genotyping.

[Click here to download Table S7](#)

Table S8. Plasmids used in this study

Plasmid	Cloning approach	Source	Purpose
pLF3FShC	N/A	Nonet, 2020	Integration vector for RMCE
pJW849	Gibson	This study	<i>wrt-2p::NLS-mScarlet (dpi)::tbb-2 3'UTR</i> promoter reporter
pJW1841	N/A	Ashley et al., 2021	promoterless <i>NLS::mScarlet (dpi)::tbb-2 3'UTR</i> vector
pJW1940	Gibson	This study	<i>SCMp::NLS-mScarlet (dpi)::tbb-2 3'UTR</i> promoter reporter
pJW2172	N/A	Ashley et al., 2021	30xlinker:mNeonGreen (dpi)::3xFLAG::10xlinker repair template
pJW2247	Gibson	This study	Promoterless <i>rde-1 CDS+3'UTR</i> in RMCE integration vector. Linearize vector with BsiWI and AvrII double digestion to Gibson clone in new promoters
pJW2236	Gibson	This study	<i>SCMp::rde-1 CDS+3'UTR</i> in RMCE integration vector for seam cell-specific RNAi
pJW2264	Gibson	This study	<i>semo-1p::rde-1 CDS+3'UTR</i> in RMCE integration vector for hypodermis-specific RNAi